

3D marine magnetotelluric modeling and inversion with the finite-difference time-domain method

Sébastien de la Kethulle de Ryhove¹ and Rune Mittet¹

ABSTRACT

Frequency-domain methods, which are typically applied to 3D magnetotelluric (MT) modeling, require solving a system of linear equations for every frequency of interest. This is memory and computationally intensive. We developed a finite-difference time-domain algorithm to perform 3D MT modeling in a marine environment in which Maxwell's equations are solved in a so-called fictitious-wave domain. Boundary conditions are efficiently treated via convolutional perfectly matched layers, for which we evaluated optimized parameter values obtained by testing over a large number of models. In comparison to the typically applied frequency-domain methods, two advantages of the finite-difference time-domain method are (1) that it is an explicit, low-memory method that entirely avoids the solution of systems of linear equations and (2) that it allows the computation of the electromagnetic field unknowns at all frequencies of interest in a single simulation. We derive a design criterion for vertical node spacing in a nonuniform grid using dispersion analysis as a starting point. Modeling results obtained using our finite-difference time-domain algorithm are compared with results obtained using an integral equation method. The agreement was found to be very good. We also discuss a real data inversion example in which MT modeling was done with our algorithm.

INTRODUCTION

In geologic environments in which seismic imaging is challenging, e.g., below highly heterogeneous basalt layers or in the presence of complex salt structures with vertical boundaries or intrasalt inclusions, magnetotelluric (MT) data can be a very useful complement to seismic data. In such situations, MT data can be used to

improve velocity models for further seismic processing or used in workflows for joint inversion and/or joint interpretation. The resistivity measurements provided by the MT method are then often found to be a useful complement to the elastic properties seismic data are sensitive to (Hovertsen et al., 1998; Key et al., 2006; Avdeeva et al., 2012; Medina et al., 2012).

In the MT method, measurements of the fluctuations in the earth's natural electromagnetic fields at several locations are used as a means to investigate the earth's resistivity structure. This is typically done by estimating frequency-dependent-impedance tensors \mathbf{Z} such that

$$\begin{pmatrix} E_x \\ E_y \end{pmatrix} = \begin{pmatrix} Z_{xx} & Z_{xy} \\ Z_{yx} & Z_{yy} \end{pmatrix} \begin{pmatrix} H_x \\ H_y \end{pmatrix} \quad (1)$$

from orthogonal measurements of horizontal electric (E_x, E_y) and magnetic (H_x, H_y) fields at the measurement sites. The magnitudes — usually converted to apparent resistivities — and phases of the components of the impedance tensor are in turn used to characterize the earth's resistivity structure. Reviews of the MT method are given by Orange (1989) and Vozoff (1991). The marine MT case, in which the measurement sites are located on the seafloor, is discussed, for example, by Constable et al. (1998), Hovertsen et al. (1998), and Key (2003, 2012).

To obtain numerical solutions to the 3D MT forward problem, one can use methods belonging to one of three main categories: finite-difference methods, finite-element methods, and integral equation methods. Algorithms based on these methods for solving the MT forward problem that can be found in the literature (Wannamaker, 1991; Mackie et al., 1993; Smith, 1996; Newman and Alumbaugh, 2000; Sasaki, 2001; Farquharson and Oldenburg, 2002; Hursan and Zhdanov, 2002; Siripunvaraporn et al., 2002; Mitsuhata and Uchida, 2004; Farquharson and Miensoopust, 2011) typically start from a frequency-domain formulation of Maxwell's equations. Discretizing the problem then leads, for each frequency of interest, to a system of linear equations that must be solved to obtain the unknown electromagnetic field values. Spectral techniques (Druskin

Manuscript received by the Editor 5 March 2014; revised manuscript received 4 June 2014; published online 8 October 2014.

¹Electromagnetic Geoservices (EMGS) ASA, Trondheim, Norway. E-mail: sryhove@emgs.com; rm@emgs.com.

© 2014 Society of Exploration Geophysicists. All rights reserved.

and Knizhnerman, 1988, 1994; Carcione, 2006) are a promising alternative that has been successfully applied to the solution of electromagnetic diffusion problems discretized with finite differences. They allow time-domain modeling without explicit time stepping. The spectral Lanczos decomposition method (Druskin and Knizhnerman, 1988, 1994) is a powerful method that also allows us to perform — in addition to time-domain modeling — frequency-domain modeling for several frequencies in one run. A review of the finite-difference and finite-element methods for geoelectromagnetics is given by Börner (2010).

In this paper, we present a method to obtain numerical solutions to the 3D MT forward problem by using the finite-difference time-domain (FDTD) method to solve Maxwell's equations in a so-called fictitious-wave domain. These equations are obtained by applying the correspondence principle for wave and diffusion fields (de Hoop, 1996) to Maxwell's equation in the diffusive limit relevant for MT exploration. The idea of solving diffusive electromagnetic problems with the FDTD method by considering an associated problem with a fictitious wavefield is first introduced by Lee et al. (1989). The respective properties of the diffusive and fictitious-wave domain fields are discussed in detail by Mittet (2010).

In comparison to the frequency-domain methods that are typically applied, two advantages of the FDTD method are immediately obvious. First, the FDTD method is an explicit method with low memory requirements in which the solution of systems of linear equations is entirely avoided. Efficiently solving linear systems of equations has been recognized as one of the main difficulties in the application of frequency-domain methods (Avdeev, 2005). Using iterative solvers (see, e.g., Sleijpen and Fokkema [1993], Table 3.1) with a finite-difference frequency-domain solver leads to memory requirements that are significantly higher than those of the FDTD method. As an illustration, to solve an $N \times N$ system of linear equations, the frequency-domain method described by Weiss and Constable (2006) in the context of controlled-source electromagnetic (CSEM) modeling leads to memory requirements of $10N$ complex, double-precision words. In comparison, the memory requirements for an FDTD method applied to a system with the same number of nodes is of the order of $2N$ real, single-precision words. A second advantage is that a single FDTD simulation allows computation of the electromagnetic field unknowns at all frequencies of interest, as opposed to frequency-domain methods that must usually be run once for each frequency of interest. Noting that one is typically interested in computing MT responses for six to 10 frequencies per decade (Simpson and Bahr, 2005), this can lead to significant computational savings. From a parallel computing perspective, frequency-domain methods in which one linear system is solved for each frequency of interest have the advantage of being embarrassingly parallel. The FDTD method is sequential in nature. It can be parallelized, although doing so efficiently requires some care (Woods et al., 2010; Cessenat, 2013). The strength of the FDTD method here is that MT modeling results for an entire survey can be efficiently obtained with only two processors (one for each polarization) and very little memory.

The transformation of Maxwell's equations from the diffusive domain to the fictitious-wave domain is performed because it allows us to significantly reduce the number of FDTD time steps that is required to obtain an accurate solution. Indeed, as pointed out by Oristaglio and Hohmann (1984), the solution to Maxwell's equations in the diffusive limit depends on events that take place at very

different time scales. Naive application of the FDTD scheme therefore leads to the use of a very small time step for a very long time, and consequently, to a prohibitively large number of time steps. Maxwell's equations in the diffusive limit are stiff. However, in the fictitious-wave domain, it is a hyperbolic system of partial differential equations that is solved, which allows the use of a comparatively large time step (Mittet, 2010). Although diffusive electromagnetic problems have been solved in this way since the late 1980s (Lee et al., 1989), it is only more recently that the large possible gains in CPU time became fully apparent (Maaø, 2007; Mittet, 2010).

We have developed an FDTD algorithm for MT modeling in a marine environment. In this paper, we do the following: First, we examine the mathematic transformation from the diffusive Maxwell equations to Maxwell's equations in the fictitious-wave domain. We then provide a description of our FDTD marine MT modeling algorithm. The focus here is on the treatment of boundary conditions and that of nonuniform grids. A key element in our handling of boundary conditions is the use of convolutional perfectly matched layers (CPMLs) (Roden and Gedney, 2000). We subsequently analyze the stability and dispersion properties of our modeling algorithm, and we propose a design criterion for vertical node spacing in nonuniform grids. MT responses computed with our algorithm are thereafter compared with results obtained with an integral equation method. The agreement is found to be very good. Finally, we discuss a real data inversion example in which our algorithm is used to perform MT modeling.

THEORY

In this section, we discuss how the diffusive Maxwell equations can be reformulated in an equivalent fictitious-wave domain. Applying Yee's (1966) FDTD scheme to the equivalent fictitious-wave domain problem rather than the original diffusive problem is advantageous in terms of computational complexity as discussed in the Introduction.

Mappings between the time and frequency domains will be accomplished via the Fourier transform:

$$F(\omega) = \int_{-\infty}^{\infty} f(t)e^{i\omega t} dt, \quad (2)$$

and its inverse,

$$f(t) = \frac{1}{2\pi} \int_{-\infty}^{\infty} F(\omega)e^{-i\omega t} d\omega, \quad (3)$$

with $i = \sqrt{-1}$.

In the diffusive limit relevant for MT exploration, Maxwell's equations read

$$\nabla \times \mathcal{E} = -\mu \partial_t \mathcal{H} - \mathcal{K}, \quad (4)$$

$$\nabla \times \mathcal{H} = \sigma \mathcal{E} + \mathcal{J}. \quad (5)$$

Here, ∂_t denotes partial differentiation with regard to time, \mathcal{E} and \mathcal{H} are the electric and magnetic fields, \mathcal{J} and \mathcal{K} denote the electric and magnetic current densities of external sources, σ is the electric conductivity tensor, and μ is the magnetic permeability tensor.

Henceforth, it will be assumed that σ is diagonal. Moreover, because the magnetic permeability of most rocks only differs little from that of free space (Nabighian, 2006), we will assume that the magnetic permeability tensor is diagonal with elements equal to $\mu_0 = 4\pi \times 10^{-7}$ H/m.

The quantities \mathcal{E} , \mathcal{H} , \mathcal{J} , and \mathcal{K} are 3D vectors that are functions of position $\mathbf{x} = (x, y, z)$ and time t . In general, the calligraphic font is reserved for functions of time, e.g., $\mathcal{E}(\mathbf{x}, t)$, $\mathcal{E}_y(\mathbf{x}, t)$, whereas a different type of font, e.g., $\mathbf{E}(\mathbf{x}, \omega)$, $E_y(\mathbf{x}, \omega)$, is reserved for frequency-domain quantities. Let $\mathcal{G}^{E|J}(\mathbf{x}, t|\tilde{\mathbf{x}})$ denote the diffusive Green's tensor function of rank two relating a point electric excitation at position $\tilde{\mathbf{x}}$ and time $t = 0$ to the resulting electric field at position \mathbf{x} and time t , and let $\mathcal{G}^{E|K}$, $\mathcal{G}^{H|J}$, and $\mathcal{G}^{H|K}$ be similarly defined. All sources $\mathcal{J}(\tilde{\mathbf{x}}, t)$ and $\mathcal{K}(\tilde{\mathbf{x}}, t)$ are assumed to vanish for $t \leq 0$.

The electromagnetic wave-propagation problem in a lossless medium is governed by equations analogous to equations 4 and 5 in the wave domain; i.e.,

$$\nabla \times \mathcal{E}' = -\boldsymbol{\mu}' \partial_t \mathcal{H}' - \mathcal{K}', \quad (6)$$

$$\nabla \times \mathcal{H}' = \boldsymbol{\epsilon}' \partial_t \mathcal{E}' + \mathcal{J}'. \quad (7)$$

The primes are used to distinguish the quantities in equations 6 and 7 from those in equations 4 and 5. Here, let the permittivity tensor $\boldsymbol{\epsilon}'$ be chosen such that

$$\boldsymbol{\epsilon}' = \frac{\boldsymbol{\sigma}}{2\omega_0}, \quad (8)$$

with $\boldsymbol{\sigma}$ being the conductivity tensor from equation 5 and $\omega_0 \in \mathbb{R}^+$ being an arbitrary angular frequency and let the permeability tensor $\boldsymbol{\mu}' = \boldsymbol{\mu}$. Moreover, let $\mathcal{G}'^{E,H|J,K}$ denote the wavefield Green's tensors analogous to those from the diffusive case defined above. Equations 6 and 7 will hereafter be said to be in the fictitious-wave domain.

Let us now show how to compute, e.g., the quantity $E_x(\tilde{\mathbf{x}}, \omega)$ from the diffusive problem of equations 4 and 5 resulting from a current source $\mathcal{J}_x(\tilde{\mathbf{x}}, t)$ by using a fictitious-wave domain FDTD scheme. The procedure is to apply Yee's FDTD scheme to equations 6 and 7 in the presence of a fictitious-wave-domain source $\mathcal{J}'_x(\tilde{\mathbf{x}}, t')$, which allows us to obtain $\mathcal{E}'_x(\mathbf{x}, t') = \mathcal{G}'^{E|J}(\mathbf{x}, t'|\tilde{\mathbf{x}}) * \mathcal{J}'_x(\tilde{\mathbf{x}}, t')$. In Appendix A, we derive expressions for the Green's tensors from the diffusive problem $\mathbf{G}^{E,H|J,K}(\mathbf{x}, \omega|\tilde{\mathbf{x}})$ that we are ultimately interested in as a function of the fictitious-wave-domain Green's tensors $\mathcal{G}'^{E,H|J,K}(\mathbf{x}, t'|\tilde{\mathbf{x}})$ using the work of de Hoop (1996) as a starting point. This establishes that using equations 6 and 7 as a starting point to compute diffusive Green's tensors keeps all the characteristics of the physics governing equations 4 and 5. If the current source $\mathcal{J}_x(\tilde{\mathbf{x}}, t)$ appearing in the system of equations 4 and 5 has a spectrum such that

$$J_x(\tilde{\mathbf{x}}, \omega) = \sqrt{\frac{-2\omega_0}{i\omega}} \int_{t'=0}^{\infty} \mathcal{J}'_x(\tilde{\mathbf{x}}, t') e^{-\sqrt{\omega\omega_0}t'} e^{i\sqrt{\omega\omega_0}t'} dt', \quad (9)$$

it can be shown, starting from the last equality in chain A-4 and following the same steps as in the proof of the convolution theorem for Fourier transforms, that

$$E_x(\mathbf{x}, \omega) = \int_{t'=0}^{\infty} \mathcal{E}'_x(\mathbf{x}, t') e^{-\sqrt{\omega\omega_0}t'} e^{i\sqrt{\omega\omega_0}t'} dt'. \quad (10)$$

In other words, the quantities $E_x(\mathbf{x}, \omega)$ and $\mathcal{G}'^{E|J}(\mathbf{x}, t|\tilde{\mathbf{x}})$ that we are interested in can be obtained by numerically computing the integrals in equations 9 and 10 on the fly as the fictitious-wave-domain FDTD scheme is applied. A similar procedure can be used to compute all components of the diffusive Green's tensors $\mathbf{G}^{E,H|J,K}(\mathbf{x}, \omega|\tilde{\mathbf{x}})$. Moreover, relations such as equation 10 can be established for all other electromagnetic fields of interest using the expressions from Appendix A as a starting point.

FDTD IMPLEMENTATION

The main idea behind our algorithm is to apply Yee's FDTD scheme (Yee, 1966) to equations 6 and 7 and use relations such as equation 10 to compute the physical fields. There are, however, some challenges. The first is related to boundary conditions, and the second to the use of nonuniform grids. We now discuss these challenges in turn.

Boundary conditions

Grid termination and MT source implementation

Let us consider the use of an FDTD method based on Yee's discretization of Maxwell's equations on a rectangular parallelepiped domain $\Omega \subset \mathbb{R}^3$, with an associated grid Ω_N consisting of a Cartesian product of 1D grids. To compute the required spatial finite differences centered around a node located on one of the outermost planes of Ω_N , knowledge of field values for "ghost" nodes that do not belong to Ω_N is required (see Figure 1). Such knowledge is by definition not available in the FDTD scheme and must be set independently. Note that the different layers of ghost nodes in Figure 1 contain nodes of different types. This is because Yee's FDTD scheme leads to different node types on the different outermost planes of Ω_N . For example, the leftmost (rightmost) plane of Ω_N contains nodes of types \mathcal{H}'_x , \mathcal{E}'_y , and \mathcal{E}'_z (\mathcal{E}'_x , \mathcal{H}'_y , and \mathcal{H}'_z). On the leftmost plane of Ω_N ,

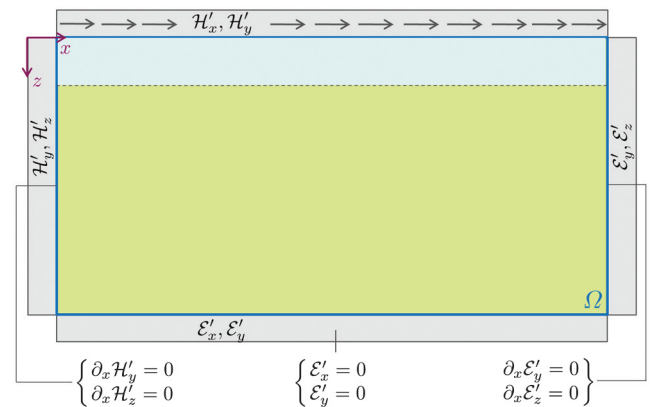


Figure 1. Original computational domain Ω (solid blue rectangle). The arrows on top of the figure denote the plane-wave MT source. The blue and green areas of Ω represent water and formation, respectively. The gray zones denote regions with "ghost" nodes that are not updated by the FDTD scheme, but to which specific field values must be assigned at each time step to be able to carry out the FDTD simulation. The node types that are present inside each gray zone have been explicitly written.

updating, e.g., an \mathcal{E}'_z node via Yee's FDTD scheme requires knowledge of $\partial_y \mathcal{H}'_z$, which can be obtained without any trouble, and of $\partial_x \mathcal{H}'_y$, for which knowledge of \mathcal{H}'_y on the leftmost layer of ghost nodes is needed (Figure 1).

We assign to the \mathcal{H}'_x and \mathcal{H}'_y ghost nodes above the top boundary of Ω a sum of two components: (1) a plane-wave MT source excitation $\mathcal{H}'_{x,MT}$ or $\mathcal{H}'_{y,MT}$ and (2) $\mathcal{H}'_{x,air}$ and $\mathcal{H}'_{y,air}$, resulting from the air-water interface condition described below. After selecting an appropriate source waveform $S(t')$, for example, the first derivative of a Gaussian pulse (Lee et al., 1989; Mittet, 2010), e.g., an x -polarized MT source would be implemented by setting $\mathcal{H}'_{y,MT}(\mathbf{x}, t') = S(t')$ in the top layer of ghost nodes.

We compute $\mathcal{H}'_{x,air}$ and $\mathcal{H}'_{y,air}$ as described by Wang and Hohmann (1993). The essence of their approach is that, under the quasistatic assumption $\nabla^2 \mathcal{H}' = 0$ in free space, which allows one to derive values for $\mathcal{H}'_{x,air}$ and $\mathcal{H}'_{y,air}$ on the top layer of ghost nodes located at a distance h above the air-water interface using values of \mathcal{H}'_z on the air-water interface. The reader is referred to Wang and Hohmann (1993) and Mittet (2010) for further details regarding this procedure.

We assign values to the vertical layers of ghost nodes via the following requirement: All electromagnetic field normal derivatives that need to be evaluated at the vertical boundaries of Ω should be identically zero. This is illustrated on the left and right sides of Figure 1 for the case of the x -direction. The intuition behind this condition is that for a 1D layered earth and a plane-wave MT source, the derivatives with regard to x and y of all quantities appearing in equations 6 and 7 are identically zero. In this case, assigning the values of the vertical layers of ghost nodes as just explained does not lead to any inaccuracies. Finally, the bottom \mathcal{E}'_x and \mathcal{E}'_y ghost nodes are set to zero.

Convolutional perfectly matched layer absorbing boundary conditions

Assigning values to the vertical and bottom layers of ghost nodes as described above introduces two sources of error. First, electro-

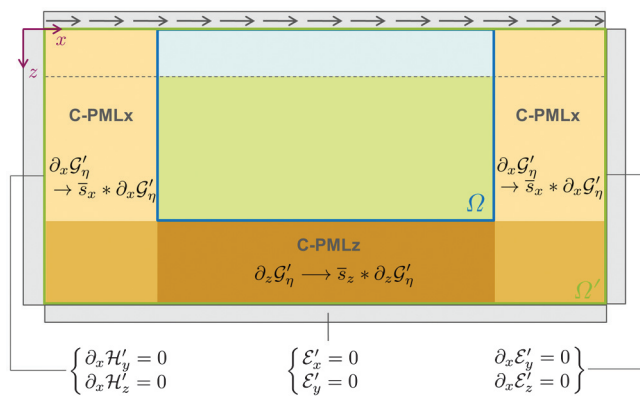


Figure 2. The original computational domain Ω (solid blue rectangle, also depicted in Figure 1) and the computational domain Ω' (solid green rectangle) after the addition of vertical and bottom CPMLs (brown areas) outside Ω . The gray zones denote regions with ghost nodes that are not updated by the FDTD scheme and correspond exactly to the gray zones from Figure 1. Note that the CPML layers (1) have been introduced between the original computational domain Ω , which remains unchanged, and the ghost nodes and (2) are not to scale and in reality are thin compared to Ω .

magnetic propagation governed by equations 6 and 7 is lossless. When the energy coming from the plane-wave MT source reaches the bottom boundary of Ω , the electromagnetic fields will thus have high amplitudes. Setting the values of the bottom \mathcal{E}'_x and \mathcal{E}'_y ghost nodes to zero is then clearly not appropriate.

Second, if there are 2D or 3D inhomogeneities in Ω , some of which may be in the vicinity of some of its vertical boundaries, the x and y derivatives of quantities appearing in equations 6 and 7 will cease to vanish at all times. Hence, assigning values to the vertical layers of ghost nodes by requiring that derivatives with regard to x and y vanish at all times will again lead to inaccuracies.

We address both of these issues by extending the vertical and bottom boundaries of Ω with CPML absorbing boundary conditions (ABCs) (see Figure 2). CPMLs provide a very powerful implementation of reflectionless ABCs for FDTD schemes (Roden and Gedney, 2000), to the extent that numerical reflections due to ABCs are no longer considered a limiting factor in the performance of FDTD schemes.

We now briefly review the CPML method on a uniform Yee grid. Let us consider a CPML, which can be up to tens of cells thick, for direction ξ extending from $\xi = 0$ to $\xi = \delta_\xi$, where δ_ξ is the CPML thickness in direction ξ and ξ is one of $\{x, y, z\}$. A complex stretching variable,

$$s_\xi(u, \omega') = \alpha_\xi(u) + \frac{\sigma_\xi(u)}{\tau_\xi(u) - i\omega' \epsilon'_\xi}, \quad (11)$$

is introduced for $0 \leq u \leq \delta_\xi$. Here, ω' is used to denote the angular frequency in accordance with previously introduced notation because it is equations 6 and 7 that define the time-marching scheme. The scalar quantity ϵ'_ξ is related to the fictitious electric permittivity tensor ϵ' from equation 8. The functions $\alpha_\xi(u) \geq 1$, $\sigma_\xi(u) \geq 0$, and $\tau_\xi(u) \geq 0$ are real and must be designed appropriately for the resulting CPML to exhibit the desirable absorption properties. Our choices for ϵ'_ξ and the functions $\alpha_\xi(u) \geq 1$, $\sigma_\xi(u) \geq 0$, and $\tau_\xi(u) \geq 0$ are discussed further in Appendix B.

In the stretched coordinate space (Chew and Weedon, 1994), the x -projection of the Fourier transform of equation 7 reads,

$$\frac{1}{s_y} \partial_y H'_z - \frac{1}{s_z} \partial_z H'_y = -i\omega' \epsilon'_{xx} E'_x + J'_x, \quad (12)$$

which, after performing an inverse Fourier transform, gives

$$(\bar{s}_y * \partial_y \mathcal{H}'_z) - (\bar{s}_z * \partial_z \mathcal{H}'_y) = \epsilon'_{xx} \partial_t E'_x + J'_x, \quad (13)$$

where $*$ denotes convolution and \bar{s}_ξ is the inverse Fourier transform of $1/s_\xi$. This corresponds to the x -projection of equation 7 in the stretched coordinate space. Similar relations for the y - and z -projections of equation 7 and all three components of equation 6 can be obtained in the same way. Updated equations for \mathcal{E}'_x , \mathcal{E}'_y , \mathcal{E}'_z , \mathcal{H}'_x , \mathcal{H}'_y , and \mathcal{H}'_z can then be derived by replacing the spatial and temporal derivatives by finite differences as done in Yee (1966) and by using a recursive convolution technique for evaluating convolutions such as those appearing in equation 13. Such derivations can be found in, e.g., Roden and Gedney (2000) and Taflov and Hagness (2005). These derivations can be generalized to take into account nonuniform node spacing without much difficulty. As we discuss below, our FDTD MT modeling algorithm allows for nonuniform

node spacing either using the nonuniform grids from Monk and Sülli (1994) or the coordinate transformation method described by Fornberg (1988).

Let us now return to the two sources of error discussed above. Let $\Omega' \subset \mathbb{R}^3$ denote the computational domain obtained by extending the vertical and bottom boundaries of Ω with CPML ABCs (see Figure 2), and let Ω'_N be the associated grid. We first note that as long as the bottom CPML performs its absorption task well, all downward propagating electromagnetic waves should be significantly attenuated by the time they reach the lowermost plane of Ω'_N , meaning that no significant errors will be introduced if the values \mathcal{E}'_x and \mathcal{E}'_y of the bottom ghost nodes are set to zero.

Let us next turn our attention to the vertical layers of ghost nodes. A crucial point is that for the case of a 1D layered earth, the introduction of vertical CPML layers is fully compatible with the requirement that all derivatives with regard to x and y vanish at all times. This is the case as long as (1) the plane-wave MT source is made to extend not only above Ω but also above the vertical CPMLs as shown in Figure 2 and (2) the material properties inside the vertical CPMLs are chosen in such a way that ϵ' is independent of x and y , not just inside Ω but also inside the whole of Ω' . Indeed, the derivatives with regard to x and y of all quantities appearing in equations 6 and 7 are then identically zero over the whole of Ω' , which in turn implies that the quantities $\bar{s}_x * \partial_x \mathcal{G}'_y$ (with \mathcal{G}'_y one of $\{\mathcal{E}'_y, \mathcal{E}'_z, \mathcal{H}'_y, \mathcal{H}'_z\}$) appearing in the x -direction CPMLs, and the corresponding quantities in the y -direction CPMLs, vanish at all times.

If in addition there are 2D or 3D inhomogeneities in Ω , possibly even in the neighborhood of some of its vertical boundaries, then as long as the vertical CPMLs perform their absorption tasks well, any electromagnetic modes exhibiting x or y dependencies should be significantly attenuated by the time they reach the vertical outer boundaries of Ω' . Hence, when computing spatial finite differences on the vertical outermost planes of Ω'_N , no significant errors will be introduced if the vertical layers of ghost nodes are assigned values using the previously described zero normal derivative conditions.

It is well known that the performance of CPML ABCs is worst when energy propagates from the computational domain into a CPML absorbing layer at close to grazing incidence (i.e., when $\theta_i \approx 90^\circ$). This issue is entirely avoided for the downgoing source field by (1) designing the MT source and vertical CPML layers as described above and (2) assigning values to the vertical layers of ghost nodes as described above.

Note that, as the original diffusive problem has been transformed to the fictitious-wave domain, the electromagnetic fields \mathcal{E}' and \mathcal{H}' have wavelike characteristics and their propagation is lossless. Hence, extending Ω by adding stretched cells at the vertical and bottom boundaries, as is often done when directly computing diffusive fields \mathcal{E} and \mathcal{H} , which attenuate rapidly in space, is not appropriate here. Indeed, because the fictitious-wave-domain fields would not undergo any attenuation when propagating through the stretched boundaries, we see, e.g., that once the energy from the plane-wave MT source reaches the vicinity of the bottom layer of ghost nodes, it would do so with high amplitude, which would lead to inaccuracies as the values of the bottom \mathcal{E}'_x and \mathcal{E}'_y ghost nodes are set to zero.

Nonuniform grids

Consider the grid design guidelines given in chapter 6 of Simpson and Bahr (2005) for finite-difference MT modeling. Whereas

the extent of the computational domain in each horizontal direction is recommended to be at least six times the longest skin depth, the node separation in the more sensitive areas of the computational domain should not exceed a quarter of the shortest skin depth. The skin depth δ at angular frequency ω in an isotropic medium with conductivity σ and permeability μ is $\delta = (\mu\omega\sigma/2)^{-1/2}$. If the node spacing in the x - and y -directions is kept constant and one models four frequency decades, the number of nodes in each horizontal direction then has to be at least $6/0.25 \times \sqrt{10^4} = 2400$. In addition, if the node spacing in the z -direction is also kept constant and one discretizes the earth over a vertical distance that spans three electromagnetic skin depths, this would lead to a 3D MT modeling grid containing at least $2400 \times 2400 \times 1200 \approx 6.9 \times 10^9$ nodes and, hence, to very high memory and computational requirements. Therefore, if one wishes to use one unique grid to produce modeling results over the entire frequency range of interest while keeping memory and complexity requirements reasonable, the usual approach when using finite differences is to use nonuniform orthogonal grids and allow the node separation to vary as a function of position in the computational domain.

There are several ways in which we could allow for nonuniform node spacing in our FDTD MT modeling algorithm. One possibility is to use the nonuniform grid presented by Monk and Sülli (1994). For such a grid, even though at nodes close to grid irregularities the finite-difference approximations are accurate only to the first order, globally Yee's scheme is second order convergent, a phenomenon that is usually referred to as *supraconvergence* (Monk and Sülli, 1994). Another possibility is to use the coordinate transformation method described by Fornberg (1988) with "real"-world mutually orthogonal coordinate axes. An advantage of the latter method is the ease with which high-order spatial differential operators can be introduced. We implemented both alternatives. For ease of exposition, the discussions in this section and the next are written with the nonuniform grid from Monk and Sülli (1994) in mind. Specific matters related to high-order differential operators and the coordinate transformation method are discussed in Appendix C.

STABILITY, DISPERSION, MEMORY, AND COMPUTATIONAL COMPLEXITY

In this section, we discuss the stability, dispersion, and the memory and computational complexity requirements associated with our FDTD algorithm. A stability criterion valid for the nonuniform grid from Monk and Sülli (1994) was derived for the case of isotropic media by Edelvik et al. (2004), according to which the time step $\Delta t'$ must satisfy

$$\Delta t' < \min_k \frac{1}{\sqrt{\frac{2\omega_0}{\mu\sigma_k} \sqrt{\frac{1}{\Delta x_k^2} + \frac{1}{\Delta y_k^2} + \frac{1}{\Delta z_k^2}}}}, \quad (14)$$

where index k runs over all the cells in the earth conductivity model, Δx_k , Δy_k , and Δz_k are the lengths of the electric field edges associated with cell k , and σ_k is the conductivity of cell k . In case the conductivity tensor corresponding to cell k is diagonal but anisotropic, we conservatively set $\sigma_k = \min\{\sigma_{k,xx}, \sigma_{k,yy}, \sigma_{k,zz}\}$. Stability for the case of the coordinate transformation method and high-order spatial differential operators is discussed in Appendix C.

The amount of numerical dispersion associated with our FDTD algorithm for a real-world angular frequency ω_a is discussed in Appendix D. The case considered there is that of an isotropic half-space with conductivity $\sigma = 2\omega_0\epsilon'$, an FDTD grid with uniform spacing Δz , a time step $\Delta t'$, and an x -polarized plane-wave source excitation at $z = 0$. If the dispersion error for a receiver measuring $E_x(z, \omega_a)$ located at $z = z_0$ is to be bounded by $\gamma > 0$ in the sense of equations D-10 and D-11, it is also shown in that Appendix D that the spacing Δz in the interval $z_0 \leq z \leq z_0 + m\delta(\omega_a)$ should satisfy requirement D-16, also stated here for convenience:

$$\Delta z < \sqrt{\frac{6\gamma}{m} \delta^2(\omega_a) + (c_\sigma \Delta t')^2}. \quad (15)$$

Here, $\delta(\omega_a)$ is the skin depth at angular frequency ω_a in the half-space with conductivity σ , $c_\sigma = \sqrt{2\omega_0/\mu\sigma}$ is the propagation velocity through this half-space, and m is a constant that can be set equal to two (see Appendix D). In the derivation of condition 15, it is assumed that a perfect electromagnetic reflector is embedded in the half-space at depth $z_0 + m\delta(\omega_a)$; see Appendix D for details. Clearly, as ω_a decreases, $\delta(\omega_a)$ increases, the interval $z_0 \leq z \leq z_0 + m\delta(\omega_a)$ over which condition 15 must hold becomes larger, but so does the maximum allowed vertical spacing Δz . Hence Δz can be gradually increased as a function of depth. Condition 15 always holds whenever

$$\Delta z < \sqrt{\frac{6\gamma}{m} \delta(\omega_a)}, \quad (16)$$

which in general is not too much stricter a requirement because it often is the case that $(c_\sigma \Delta t')^2 \ll 6\gamma \delta^2(\omega_a)/m$. Also, because condition 16 does not depend on c_σ or $\Delta t'$, it is easier to use than condition 15. Conditions 15 and 16 can be very useful design criteria. Note that condition 15 can also be used with finite-difference frequency-domain modeling schemes simply by setting $\Delta t' = 0$, which actually leads to condition 16, as in such schemes there is no temporal dispersion.

For a general 3D earth model $\sigma(x, y, z)$, dispersion analysis is more complex. One possibility to find appropriate vertical spacings Δz as a function of depth is to compute $\sigma_{\max} = \max_{x,y,z} \sigma(x, y, z)$ and $\sigma_{\min} = \min_{x,y,z} \sigma(x, y, z)$. In order for dispersion to be small for a receiver measuring $E_x(z, \omega_a)$ located at $z = z_0$, condition 15 or 16 with $\sigma = \sigma_{\max}$ can then be made to hold in the interval $z_0 \leq z \leq z_0 + m\delta_{\sigma_{\min}}(\omega_a)$. If one proceeds in this fashion, the requirement from condition 15 or 16 is met over the appropriate interval for the case of a half-space with conductivity $\sigma = \sigma_{\min}$ and the case in which $\sigma = \sigma_{\max}$.

Another possibility to evaluate how suitable the vertical node spacing in a given nonuniform grid is for performing 3D MT modeling is to compare analytical solutions for MT impedances in a 1D layered earth obtained, e.g., using Wait's recursion formula (Wait, 1954; Simpson and Bahr, 2005) to impedances produced by our FDTD MT modeling scheme. When selecting 1D earth models to perform this comparison, it is desirable to include high-resistivity contrasts to reflect downward propagating waves that have undergone numerical dispersion back toward the receiver. If significant deviations are observed the grid needs to be made finer in the z -direction.

In this discussion, we have focused mostly on issues related to nonuniform node spacing in the vertical direction. MT modeling

results usually are less sensitive to horizontal variations in grid spacing as noted by Madden and Mackie (1989). For the special case of 1D earth models, modeling results are completely independent of the horizontal node spacing as the energy from a plane-wave MT source then propagates purely vertically. If horizontal conductivity contrasts are present, obliquely traveling waves will also appear and affect the modeling results, which then also become a function of the horizontal node spacing. In the latter case, consider a plane electromagnetic wave of angular frequency ω_a propagating from a horizontal conductivity contrast to a receiver location. Starting from such a wave, we can write conditions resembling equations D-10 and D-11 that should hold so as to not degrade the modeling results. Such an analysis can then be used to find guidelines to select appropriate horizontal grid spacings. In practice, simple comparisons to modeling results obtained with a fine horizontal grid spacing are probably the easiest approach to find horizontal grid spacing requirements. It is also useful to remember, as pointed out by Madden and Mackie (1989) and de Groot-Hedlin (2006), that one should be particularly careful near regions with high horizontal conductivity contrasts when selecting the horizontal node spacing.

We now briefly discuss the memory and computational complexity of our FDTD scheme. The memory requirements are of six real single-precision words for each standard FDTD cell. For each CPML cell, an additional six real single-precision words are required. For cells belonging to more than one CPML layer, the additional memory requirements for each CPML layer should be added. For example, the total memory requirement for a cell in a model corner belonging to all three x -, y -, and z -direction CPMLs is then 24 real, single-precision words. Let us now turn our attention to computational complexity. By virtue of the presence of the negative exponential in the integrand of equations such as equation 10, we see that to obtain an accurate estimate for the electromagnetic fields at an angular frequency $\omega = 2\pi/T$, it is sufficient to carry out the FDTD computations until a fictitious time $t'_{\max} \approx 4/\sqrt{\omega\omega_0} = \sqrt{T} \times 4/\sqrt{2\pi\omega_0}$. The simulation time is hence proportional to the square root of the longest period one wishes to compute MT responses for. The required number of FDTD time steps is $N_t = t'_{\max}/\Delta t'$, where $\Delta t'$ should satisfy a stability criterion such as that given in equation 14.

BENCHMARKING

In this section, we compare the results produced by our FDTD MT modeling algorithm to results produced by integral equation modeling software developed by the University of Utah Consortium for Electromagnetic Modeling and Inversion (CEMI) (Hursan and Zhdanov, 2002; Ueda and Zhdanov, 2006). For this, we use the model depicted in Figure 3, which is a slightly modified version of Dublin test model 1 (Miensopust et al., 2013). A 500-m water layer with resistivity 0.25 Ωm was added to the latter model because we are interested in marine environments. As can be seen in Figure 3, the model we use consists of three parallelepiped anomalies with resistivities of, respectively, 1 Ωm , 10 Ωm , and 1000 Ωm embedded in a homogeneous 100 Ωm half-space located under the water layer. The $79 \times 79 \times 54.5$ -km domain used for the FDTD computations is shown by the black dashed lines in Figure 3. The width in the x - and y -directions of the cells in the FDTD modeling grid was kept uniform and equal to 500 m, whereas in the z -direction, the cell thickness was of 100 m for $0 \text{ km} < z \leq 5.7 \text{ km}$; it was gradually increased from 100 m to 1 km with a ratio of approx-

imately 1.2 between adjacent cells for $5.7 \text{ km} < z \leq 10.5 \text{ km}$, and it was kept uniform and equal to 1 km for $10.5 \text{ km} < z \leq 54.5 \text{ km}$. The cell thicknesses in the z -direction will be discussed further below. This gave a total of $158 \times 158 \times 113$ cells excluding CPML layers and of $178 \times 178 \times 123 \approx 3.897 \times 10^6$ cells including 10-cell-thick CPML layers.

Apparent resistivity $\rho_{ij} = \frac{|Z_{ij}|}{\mu_0 \omega}$ and phase $\phi_{ij} = \arg Z_{ij}$ values produced by our FDTD algorithm, with nonuniform node spacing in the z -direction implemented using the nonuniform grid from Monk and Stülli (1994), are compared to results from integral equation modeling software developed by CEMI in Figures 4 and 5. Figure 4 shows plots as a function of the period T for the receiver marked with a yellow circle in Figure 3. Figure 5 is along the profile marked with the blue line in Figure 3 for $T = 1000 \text{ s}$. Following common practice, the phases ϕ_{xy} and ϕ_{yx} have been plotted in the same quadrant for compactness. Note that our algorithm produced accurate results for long periods (see Figures 4 and 5) in spite of the

limited vertical extent of the FDTD computational domain. For example, for $T = 1000 \text{ s}$, the skin depth in the $100\text{-}\Omega\text{m}$ background is approximately 159 km, which significantly exceeds the 54.5-km vertical extent of the model. For this period, the mean deviations between the apparent resistivity (ρ_{xy} and ρ_{yx}) and phase (ϕ_{xy} and ϕ_{yx}) values computed by the FDTD and integral equation modeling algorithms were 0.50% and 0.039° , respectively. The corresponding values at $T \approx 31.6 \text{ s}$, where the skin depth in the $100\text{-}\Omega\text{m}$ background is approximately 28 km, were 0.29% and 0.045° , respectively. Going from $T \approx 31.6 \text{ s}$ to $T = 1000 \text{ s}$, there is hence an extremely small degradation in the apparent resistivity fit, whereas the phase fit, clearly also influenced by other factors and discussed further below, actually improves very slightly. This shows that the CPML ABCs performed very well. Note in addition that the FDTD modeling results remain accurate even close to the edges of the computational domain, as can be seen from Figure 4.

The deviation between the apparent resistivity (ρ_{xy} and ρ_{yx}) and phase (ϕ_{xy} and ϕ_{yx}) values computed by the FDTD and integral equation modeling algorithms always remained below 0.86% and 0.15° , respectively, for all receivers and periods. The overall agreement between the codes is hence very good. The largest phase deviations were observed at periods $T \approx 20 \text{ s}$ for receivers situated at the same time (1) above the conductivity contrast between the $1\text{-}\Omega\text{m}$ anomaly and the $100\text{-}\Omega\text{m}$ background and (2) not directly above the $10\text{-}\Omega\text{m}$ anomaly, e.g., the receiver marked with the yellow circle in Figure 3. The skin depth at $T = 20 \text{ s}$ in the $100\text{-}\Omega\text{m}$ background being of approximately 22 km, propagation inside the $1\text{-}\Omega\text{m}$ anomaly located 20 km below the seabed will bear an influence, albeit small as explained further below, on the computed MT responses for these receivers. Interestingly, the requirement from condition 15 for a half-space with conductivity $\sigma = 1 \text{ S/m}$, a period

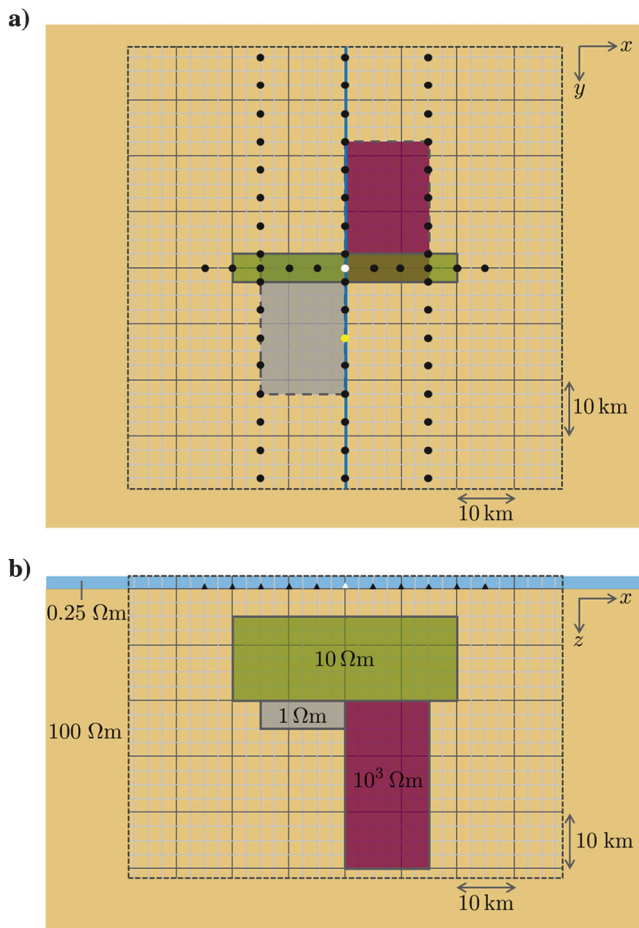


Figure 3. Model for comparing results produced by our FDTD algorithm with results from integral equation modeling software, modified after Miensoop et al. (2013). The black dashed lines show the limits of the FDTD computational domain. The water layer is 500-m thick. The solid black and gray lines are a visual aid (except for the 500-m thick water layer, the drawing is to scale). The black circles and triangles indicate receiver positions. The white circle and triangle denote a receiver with coordinates $(x, y, z) = (0, 0, 500 \text{ m})$. The receiver examined in Figure 4 is depicted with a yellow circle, whereas the profile examined in Figure 5 is marked with a blue line. (a) Plan view and (b) vertical cross section at $y = 0$.

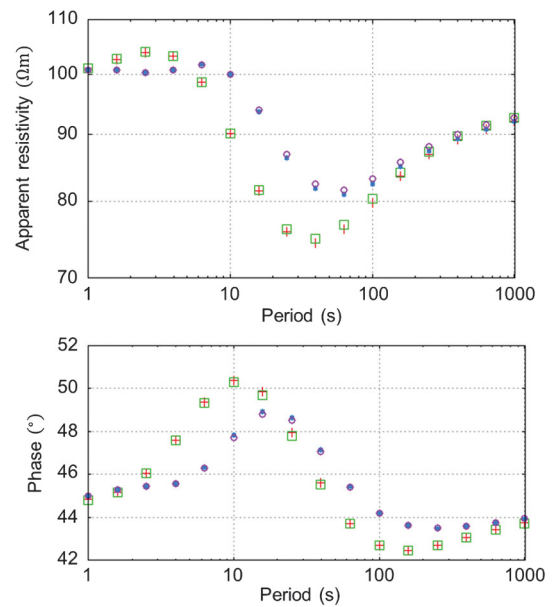


Figure 4. Apparent resistivities ρ_{xy} and ρ_{yx} (top) and phases ϕ_{xy} and ϕ_{yx} (bottom) produced by our FDTD algorithm (red crosses, xy -mode; filled blue circles, yx -mode) and by integral equation software (open green squares, xy -mode; open purple circles, yx -mode) as a function of the period T for the receiver marked with a yellow circle in Figure 3. The integral equation software was developed by CEMI (Hursan and Zhdanov, 2002; Ueda and Zhdanov, 2006).

$T = 20$ s, $\gamma = 1\%$, $m = 2$, and a choice for $\Delta t'$ close to the bound from equation 14 leads to the recommendation $\Delta z \lesssim 390$ m, whereas in the region occupied by the 1- Ω m anomaly, the vertical cell spacing is of 1 km. For comparison, we run a new set of FDTD computations in which the cell thickness in the z -direction was kept uniform and equal to 100 m for $0 \text{ km} < z \leq 54.5 \text{ km}$, and all other settings were kept unchanged. This led to a very slight improvement in the agreement between the MT responses computed by the FDTD and integral equation algorithms; e.g., the largest observed phase deviations decreased by $\sim 0.012^\circ$. The improvement here is only marginal because the influence of waves having propagated through the 1- Ω m anomaly on the final computed MT responses at $T \approx 20$ s is only small. To see this, consider a 1D earth model consisting of a 500-m water layer, a 100- Ω m background, and a 1- Ω m anomaly with now infinite extent in the x - and y -directions. Before reaching a receiver, the waves we are considering must (1) travel 20 km, i.e., almost one skin depth, through the 100- Ω m background; (2) travel 5 km, i.e., more than two skin depths, through the 1- Ω m anomaly; (3) undergo reflection at the interface located at $z = 25.5$ km, (4) travel another 5 km upward through the 1- Ω m anomaly; and finally, (5) travel 20 km upward through the 100- Ω m background. This illustrates the use of design criterion 15: running the FDTD simulations with $\Delta z = 100 \text{ m} < 390 \text{ m}$ rather than $\Delta z = 1 \text{ km} > 390 \text{ m}$ in the region occupied by the 1- Ω m anomaly led to an accuracy improvement which, as expected in this specific case, is small.

The FDTD modeling results were produced using a computer with dual Intel Xeon E5-2690 CPUs running at 2.9 GHz. We used one processor per FDTD simulation. The runtime for the grid with nonuniform spacing in the z -direction was of approximately 25 min per source polarization. Assuming that one wishes to compute MT

responses for a total of 10 periods per decade between 1 and 1000 s, this gives an equivalent runtime of approximately $\frac{25 \text{ min} \times 60}{3 \times 10^{+1}} \approx 49$ s per period per source polarization. For this hardware and our specific implementation, we also observed that FDTD computations for a CPML cell took on average 70%–80% longer than for a standard cell.

REAL DATA INVERSION EXAMPLE

The modeling scheme discussed above can be applied to the inversion of MT data. We have implemented an iterative 3D scheme based on the limited-memory Broyden-Fletcher-Goldfarb-Shanno (L-BFGS) update method (Byrd et al., 1995). To perform a model update at a given iteration, the L-BFGS software requires the misfit and the gradient of the misfit functional with respect to conductivity or resistivity. The calculation of the gradient as presented here is closely related to that given by Newman and Alumbaugh (2000).

Gradient

Let the earth be divided into P cells, let each cell be assigned horizontal and vertical conductivity values, and let \mathbf{m} be a vector of length $2P$ describing these values. The observed quantities are the four components of the impedance tensor at all receiver locations \mathbf{x}_r and angular frequencies ω . We use the error functional

$$\begin{aligned} \psi^n &= \psi_{\text{data}}^n + \lambda R(\mathbf{m}^n) \\ &= \sum_{i,j,\mathbf{x}_r,\omega} W_{ij}(\mathbf{x}_r, \omega) \Delta Z_{ij}^{n*}(\mathbf{x}_r, \omega) \Delta Z_{ij}^n(\mathbf{x}_r, \omega) + \lambda R(\mathbf{m}^n), \end{aligned} \quad (17)$$

where $i, j \in \{x, y\}$, the superscript n denotes the iteration number, the asterisk denotes complex conjugation, $\lambda \in \mathbb{R}^+$ is the Tikhonov regularization parameter, and $R(\mathbf{m}^n)$ is a regularization term. In addition,

$$\Delta Z_{ij}^n(\mathbf{x}_r, \omega) = Z_{ij}^{\text{obs}}(\mathbf{x}_r, \omega) - Z_{ij}^n(\mathbf{x}_r, \omega) \quad (18)$$

is the difference between the observed and predicted impedances at iteration n , and

$$W_{ij}(\mathbf{x}_r, \omega) = \frac{1}{\mu_0 \omega \hat{S}_{ij}^2(\mathbf{x}_r, \omega)} \quad (19)$$

is a weighting factor. Here, $\hat{S}_{ij}(\mathbf{x}_r, \omega) = \eta S_{ij}(\mathbf{x}_r, \omega)$, where $S_{ij}(\mathbf{x}_r, \omega)$ is the standard deviation of the observed data, which can vary over several decades, and η is a multiplicative factor. The factor η is chosen to be approximately the inverse of the average of $S_{ij}(\mathbf{x}_r, \omega)$, and it does not depend on the receiver number or angular frequency. It is a common factor for all data for a given MT survey. Thus, $\hat{S}_{ij}(\mathbf{x}_r, \omega)$ is dimensionless and on average of order unity. The weight function is proportional to inverse angular frequency. The effect of this is that the kernels of the error functional have the same frequency scaling as apparent resistivity $\rho_{ij} = \frac{|Z_{ij}|}{\mu_0 \omega}$. The expression for the kernel of the misfit function can be viewed as a misfit in apparent resistivity,

$$\Delta \rho_{\text{app}}^n(\mathbf{x}_r, \omega) \approx \frac{\Delta Z_{ij}^{n*}(\mathbf{x}_r, \omega) \Delta Z_{ij}^n(\mathbf{x}_r, \omega)}{\mu_0 \omega}. \quad (20)$$

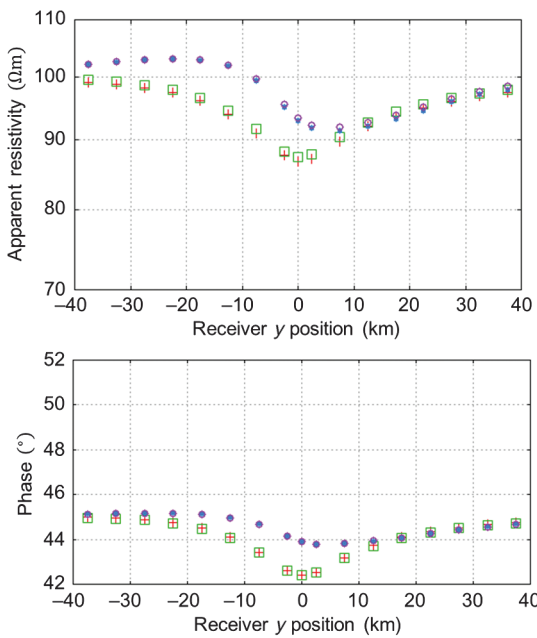


Figure 5. Apparent resistivities ρ_{xy} and ρ_{yx} (top) and phases ϕ_{xy} and ϕ_{yx} (bottom) produced by our FDTD algorithm (red crosses: xy -mode, filled blue circles: yx -mode) and by integral equation software (open green squares: xy -mode, open purple circles: yx -mode) at $T = 1000$ s along the profile $x = 0$ marked with the blue line in Figure 3. The integral equation software was developed by CEMI (Hursan and Zhdanov, 2002; Ueda and Zhdanov, 2006).

The factor η does not influence the inversion and is introduced because it gives an intuitive understanding of the size of the misfit for a given receiver at a given angular frequency. The regularization term $R(\mathbf{m})$ chosen in the example below favors horizontally smooth conductivity models \mathbf{m} by requiring that derivatives with regard to x, y be small. The Tikhonov parameter λ is adaptively tuned to give a ratio of model space error to data space error of approximately 15% for early iterations and approximately 2% for iterations $n > 100$.

The data space gradients with regard to the horizontal and vertical conductivities $m_h(\mathbf{x}_p)$ and $m_v(\mathbf{x}_p)$ of the earth model cell with center \mathbf{x}_p ($1 \leq p \leq P$) are formally

$$\begin{aligned} g^n(m_t(\mathbf{x}_p)) &= \frac{\partial \psi_{\text{data}}^n}{\partial m_t(\mathbf{x}_p)} \\ &= - \sum_{i,j,\mathbf{x}_r,\omega} W_{ij}(\mathbf{x}_r, \omega) \Delta Z_{ij}^{n*}(\mathbf{x}_r, \omega) \\ &\quad \times \frac{\partial Z_{ij}^n(\mathbf{x}_r, \omega)}{\partial m_t(\mathbf{x}_p)} + \text{c.c.}, \end{aligned} \quad (21)$$

where $t = h$ for horizontal conductivity, $t = v$ for vertical conductivity, the notation c.c. denotes the complex conjugate of the term immediately preceding it, and the data error ψ_{data}^n is defined in equation 17. With k taking on the values x and y , using the Einstein summation convention, the gradient for horizontal conductivity reads

$$g^n(m_h(\mathbf{x}_p)) = \sum_{\omega} G_{kq}^{E|J}(\mathbf{x}_p, \omega | \mathbf{x}_s) \Gamma_{kq}(\mathbf{x}_p, \omega) + \text{c.c.}, \quad (22)$$

and that for vertical conductivity

$$g^n(m_v(\mathbf{x}_p)) = \sum_{\omega} G_{zq}^{E|J}(\mathbf{x}_p, \omega | \mathbf{x}_s) \Gamma_{zq}(\mathbf{x}_p, \omega) + \text{c.c.}, \quad (23)$$

where \mathbf{x}_s is the source location and the $G_{lq}^{E|J}(\mathbf{x}_p, \omega | \mathbf{x}_s)$ for $l \in \{x, y, z\}$ are the diffusive Green's tensors introduced earlier in the theory section. The index q runs over the two horizontal polarizations of the MT source field. The gradients have the standard form of a crosscorrelation between a direct field and an adjoint field. The direct field is given by $G_{lq}^{E|J}(\mathbf{x}_p, \omega | \mathbf{x}_s)$ and the adjoint field by $\Gamma_{lq}(\mathbf{x}_p, \omega)$. The latter can be expressed as

$$\begin{aligned} \Gamma_{lq}(\mathbf{x}_p, \omega) &= \sum_{\mathbf{x}_r} [G_{lh}^{E|J}(\mathbf{x}_p, \omega | \mathbf{x}_r) \Delta J_{hq}^*(\mathbf{x}_r, \omega) \\ &\quad + G_{lh}^{E|K}(\mathbf{x}_p, \omega | \mathbf{x}_r) \Delta K_{hq}^*(\mathbf{x}_r, \omega)]. \end{aligned} \quad (24)$$

The electric dipoles $\Delta J_{hq}^*(\mathbf{x}_r, \omega)$ and the magnetic dipoles $\Delta K_{hq}^*(\mathbf{x}_r, \omega)$ depend on the impedance misfits at the receiver locations $\Delta Z_{ij}^n(\mathbf{x}_r, \omega)$; see Appendix E. Hence, in the frequency domain, two modeling operations per frequency, one for each source polarization, are required to determine the direct fields. Likewise, two modeling operations per frequency are required to determine the adjoint state fields. All the receiver locations become simultaneous source locations for the adjoint state calculation. Therefore, as an example, if the impedance tensor is given for 20 frequencies, the total number of modeling operations required to perform one iteration is 80.

This is different with the above time-domain method. The direct fields for all frequencies are determined by two modeling operations, one for each polarization. In principle, the adjoint state fields for all frequencies could also be determined by two modeling operations. However, as stated by de Hoop (1996), the transform from fictitious time to frequency is stable and unique whereas that from frequency to fictitious time is nonunique. The problem of generating proper fictitious time-domain sources from their frequency-domain counterparts is discussed in Støren et al. (2008) and Mittet (2010). Our practical experience with MT data is that groups of five frequencies can be transformed simultaneously to fictitious time. Computing the adjoint state fields therefore requires a total of eight modeling operations. Adding the two direct state simulations, we see that one iteration requires 10 modeling operations for the fictitious time-domain method. This number can be compared to the 80 simulations required for a frequency-domain method.

It is clear from equation 11 of Mittet (2010) that electric and magnetic dipole sources must be treated slightly differently if they are to appear simultaneously for the same simulations. The magnetic dipole source problem is as follows: $\forall \mathbf{x}_r$ find $K'_{hq}(\mathbf{x}_r, t')$ such that

$$\int_{t'=0}^{\infty} K'_{hq}(\mathbf{x}_r, t') e^{i\omega t'} dt' = \Delta K_{hq}^*(\mathbf{x}_r, \omega) \quad (25)$$

for five neighboring frequencies. That for electric dipoles is as follows: $\forall \mathbf{x}_r$ find $J'_{hq}(\mathbf{x}_r, t')$ such that

$$\int_{t'=0}^{\infty} J'_{hq}(\mathbf{x}_r, t') e^{i\omega t'} dt' = \sqrt{\frac{-i\omega}{2\omega_0}} \Delta J_{hq}^*(\mathbf{x}_r, \omega) \quad (26)$$

for five neighboring frequencies. Støren et al. (2008) and Mittet (2010) discuss methods for the optimization of these types of time functions. Expressions for $\Delta K_{hq}(\mathbf{x}_r, \omega)$ and $\Delta J_{hq}(\mathbf{x}_r, \omega)$ are given in Appendix E.

Real data

We applied the inversion scheme to a data set acquired in the western part of the Barents Sea in 2010. Marine CSEM and marine MT data were recorded. In total, 80 receivers were deployed in 8 south–north lines with 10 receivers each. The line and site spacing was 3 km. There were good MT data on 75 of the receivers. The remaining receivers suffered from different problems and were not included in the inversion.

The marine CSEM data were inverted first in a stand-alone inversion. This gave clear indications of subsurface high resistivity discussed further below. The MT data used in our inversions consist of impedance tensors for 17 periods per receiver ranging from 1.45 to 375 s. We had data up to $T \approx 1000$ s. However, because only depths $0 \text{ km} \leq z \leq 10 \text{ km}$ were of interest to us, the longest periods were excluded. Because the 3D MT inversion failed to converge starting from homogeneous half-space models, we first run 2D MT inversions for the eight south–north receiver lines. The software that was used for this purpose is based on 2D versions of the modeling and inversion schemes described in this paper. A 3D initial resistivity model was then generated by smooth interpolation of the 2D cross sections in the east–west direction. This 3D initial model had a high-resistivity volume with depth range 3–6 km in the central part of the receiver grid. Although the geometry of this

volume was erroneous, as is evident from the high initial data-misfit term (see Figures 6–9), this start model was still good enough to get the 3D MT inversion to converge. There were no indications of this high-resistive volume reaching the seabed from the 2D MT inversions. The north-east-depth dimensions of the 3D inversion resistivity grid were $82 \times 62 \times 20$ km. The water depth in the area is 550 m with a fairly flat seabed. The inversion domain was the whole model from the seabed and down. The x - and y -axes, respectively, coincide with the north and east directions, and the z -axis points down.

The total error as a function of iteration number is shown in Figure 6. In total, 196 iterations were performed. The total error is in black, the data-space contribution is in green, and the model-space contribution is in blue. The evolution of the total error as a function of the iteration number shows a well-known behavior with good progress at early iterations and slower progress at later iterations. The later iterations are necessary to develop the finer details of the resistivity model. It is clear from Figure 6 that the model-space contribution to the error is small at later iterations and hence that very little horizontal smoothing is enforced for the final resistivity model.

Figure 7 shows the data-space error as a function of receiver location:

$$\psi_{\text{data}}^n(\mathbf{x}_r) = \sum_{i,j,\omega} W_{ij}(\mathbf{x}_r, \omega) \Delta Z_{ij}^{n*}(\mathbf{x}_r, \omega) \Delta Z_{ij}^n(\mathbf{x}_r, \omega). \quad (27)$$

This error is shown in map view for the initial and final resistivity models. The left panel of the figure also shows the site numbering. The initial data-space error is (1) clearly largest in the central section

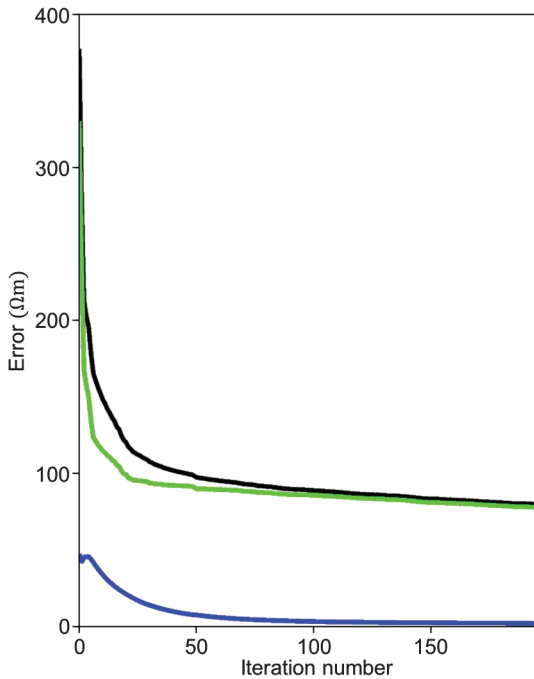


Figure 6. Total (black line), data-space (green line), and model-space (blue line) errors as a function of the iteration number. The total error is the sum of data-space and model-space errors. The data-space error is the sum of the data-space error kernel over impedance tensor components, receiver locations, and frequencies. The kernel of the misfit function can be viewed as a misfit in apparent resistivity. The error is hence measured in Ωm .

of the receiver grid and (2) higher in the east and northeast than in the west of the receiver grid. At the east and northeast of the receiver grid, the stand-alone CSEM inversion indicated high resistivity in the intermediate to shallow subsurface, which is a trend that was also confirmed in another combined CSEM-MT survey immediately to the north of the one that is discussed here. These resistive layers are not believed to be salt, and the interpretation is still open with respect to what sort of rock causes this high resistivity. The data-space error is more evenly distributed for the final resistivity model. Receiver number 68 (marked in Figure 7) has a higher misfit than the others. Some of the neighboring receivers in the northeast corner also have a final misfit that is above average. This is evident from Figure 8: in particular for the longer periods, note the color in the bottom panel for sites 63–65 and 71–75. This can be compared to the lighter color, which also gives an idea of the average misfit, for sites 1–47.

Figure 8 shows the data-space error

$$\psi_{\text{data}}^n(\mathbf{x}_r, \omega) = \sum_{i,j} W_{ij}(\mathbf{x}_r, \omega) \Delta Z_{ij}^{n*}(\mathbf{x}_r, \omega) \Delta Z_{ij}^n(\mathbf{x}_r, \omega) \quad (28)$$

as a function of the period $T = 2\pi/\omega$ for each receiver. For the initial model, we observe that the misfit is distributed over all periods except for the shortest ($T < 2$ s). An inspection of the results for the final iteration reveals that the inversion succeeded in reducing the misfit over most of the frequency band. It is clear that the remaining large misfits are for long periods. The background resistivity (i.e., that outside the high resistivity bodies) was approximately $1.2 \Omega\text{m}$ in the intermediate and deeper parts of the final model. This amounts to a skin depth of approximately 10 km for the longest period ($T = 375$ s) used in this inversion. The inversion did not increase resistivity above $1.2 \Omega\text{m}$ below depths of 6 km even after 196 iterations. If we had observed such a trend, we would have re-run the inversion using a model with a larger maximum depth. The large remaining error on receiver 68 is also for the long periods. For this receiver, we have a reasonable misfit for all impedance tensor components except Z_{yx} , for which the standard deviation is unusually large. We suspect there is a remaining noise problem related to Z_{yx} and that its standard deviation was underestimated although it is large. A higher estimate for this quantity would have diminished the contribution of Z_{yx} to the inversion itself and the final misfit.

Figure 9 shows apparent resistivity and phase curves for receivers 24 and 33 (marked in Figure 7). The black lines are for Z_{xy} , and the green lines for Z_{yx} . The contributions from the diagonal impedance tensor components Z_{xx} and Z_{yy} are small. They are not displayed in Figure 9 for the purpose of clarity but contribute to the misfits displayed in Figures 6–8. The observed data are displayed with error bars. The predicted data from the initial and final models are, respectively, displayed with dashed and solid lines. Receiver 33 is the receiver with the highest misfit for the initial model. Receiver 24, immediately to the northwest of it, also has a large initial misfit. In the inversion as a whole, it was observed that, for the final model, the agreement between the predicted and observed apparent resistivities ρ_{xy} and ρ_{yx} was typically better than for the phases ϕ_{xy} and ϕ_{yx} . For the longer periods, ϕ_{xy} has a tendency to be on the lower limit of the error bars. Moreover, the agreement between predicted and observed data was best at short and medium period lengths. However, the latter observation does not apply to the two shortest

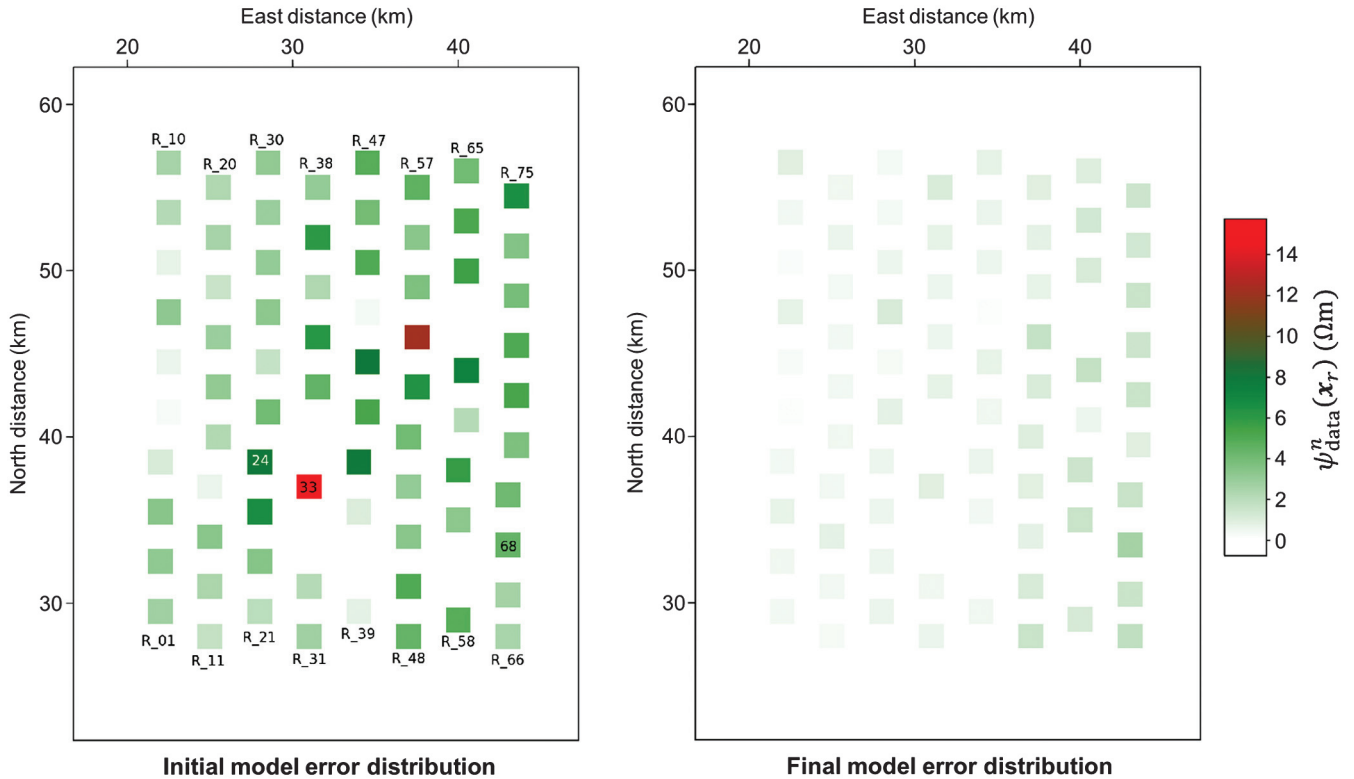


Figure 7. Data-space error ψ_{data}^n as a function of receiver location \mathbf{x}_r (see equation 27). The kernel of the misfit function can be viewed as a misfit in apparent resistivity. Hence, ψ_{data}^n is measured in Ωm .

periods for which the data have large error bars. These trends can be observed in Figure 9.

The central part of the resistivity model at the final iteration is displayed in Figure 10. The section of the model displayed here is roughly limited by the outline of the receiver grid, and it has north-east-depth dimensions of $32 \times 32 \times 20$ km. The object marked A was interpreted to be a salt layer. It is roughly 1 km thick, and it is positioned in depth from approximately 5 to 6 km, but it dips downward to the east to a maximum depth of 6.5 km. Its maximum extension in the east-west direction is 13 km, while in the south-north direction, it is 9 km. The central body, interpreted to be salt and on which a diapir can be seen, is marked B. Its maximum depth is 5.5 km, and it reaches the seabed. This salt body was also identified in the stand-alone CSEM inversion. However, the latter inversion failed to properly delineate it or to identify its bottom boundary. The shallow resistive object marked C coincides with the shallow resistivity trend identified from the CSEM inversion.

It took approximately 40 min per iteration to run the inversion on a machine with 2.9 Ghz dual Intel Xeon E5-2690 CPUs, 16 processors, and 256 GB memory. Two and eight processors, respectively, were used in parallel during the computation of the direct and adjoint fields.

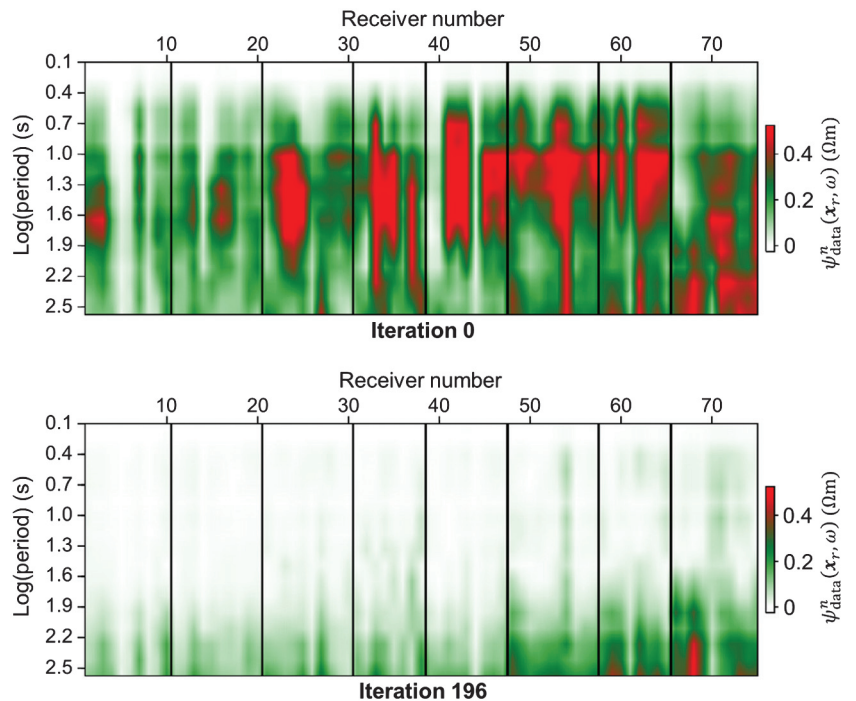


Figure 8. Data-space error ψ_{data}^n as a function of receiver location \mathbf{x}_r and period $T = 2\pi/\omega$ (see equation 28), for the start model (top) and the model after the final inversion iteration (bottom). The kernel of the misfit function can be viewed as a misfit in apparent resistivity. Hence, ψ_{data}^n is measured in Ωm .

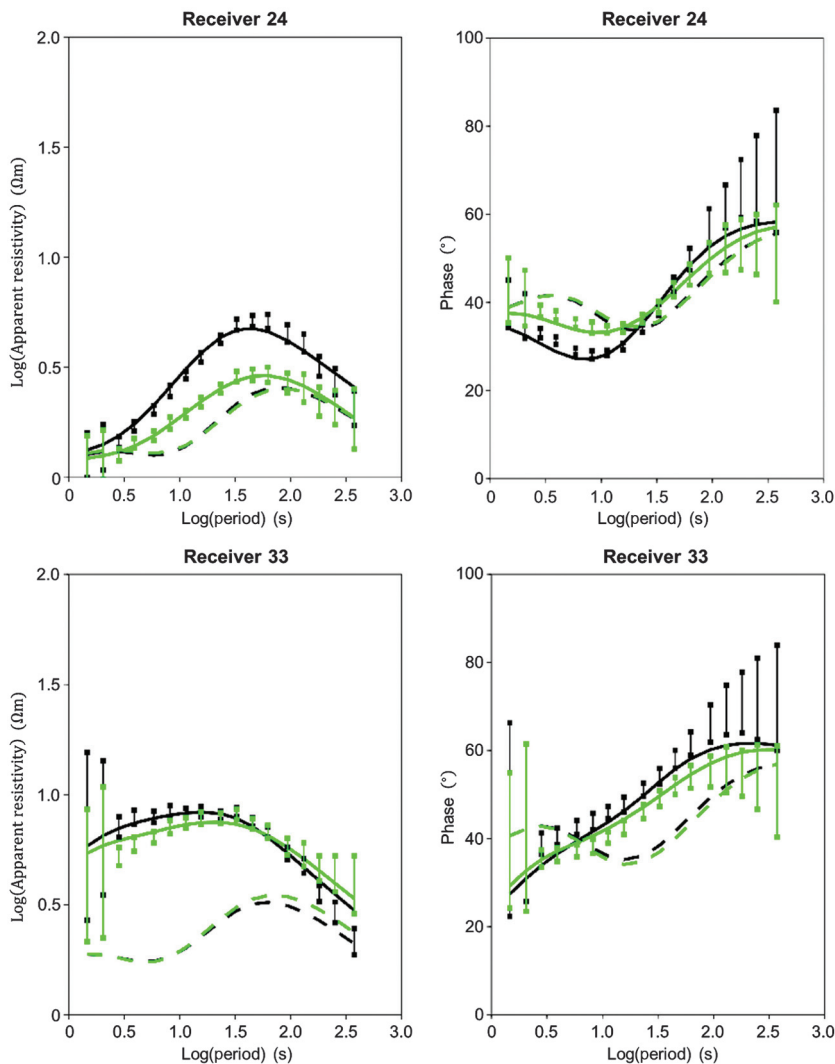
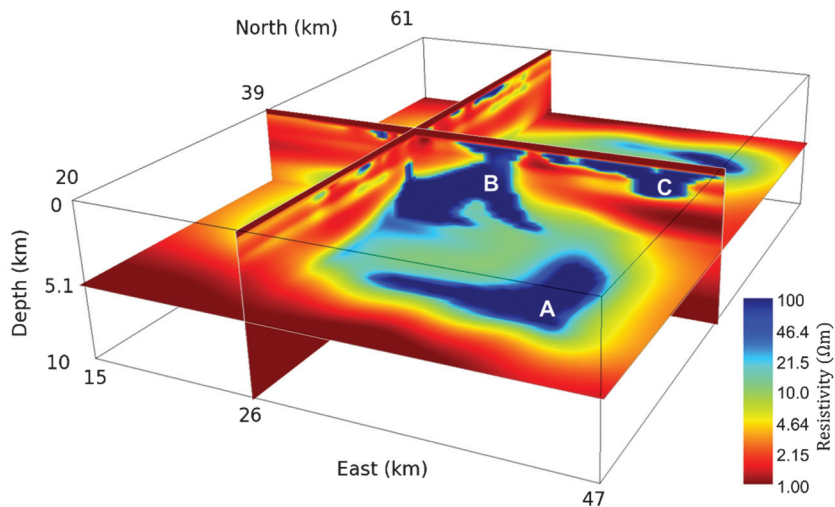


Figure 9. Apparent resistivity and impedance phase. The black lines are for Z_{xy} , and the green lines are for Z_{yx} . The observed data are displayed with error bars. The predicted data from the initial and final models are displayed with dashed and solid lines, respectively.

Figure 10. Final resistivity model from our MT inversion applied to real data from the western Barents Sea. Object A is roughly 1 km thick and was interpreted to be a salt layer. Object B is a salt body with maximum depth of 5.5 km. Object C is a shallow resistive object and agrees with the shallow resistive trend identified in a separate CSEM inversion. Below the 10-km investigation depth, the resistivity remained below $\sim 1.2 \Omega\text{m}$ and no features of interest were identified. The color scale was clipped below $1 \Omega\text{m}$ because lower resistivities only appeared in the water layer.



CONCLUSION

Applying the FDTD method in a fictitious-wave domain can be an attractive alternative for performing marine MT modeling and for inverting real-world marine MT data. Modeling results obtained with this method have been shown to be in good agreement with results produced by integral equation modeling software, and the scheme has been used to invert a 2010 data set from the Barents Sea.

Although use of the FDTD method is not widespread in marine MT modeling and inversion software today, it has some clear benefits: very low memory usage and the fact that electromagnetic field unknowns for all frequencies of interest are obtained in a single FDTD simulation. However, when using this method to compute adjoint-state fields in order to obtain the gradients required for inversion, the fact that the transform from frequency to fictitious time is nonunique causes difficulties. Our practical experience is then that electromagnetic field unknowns for only up to five frequencies can be simultaneously obtained in a single FDTD simulation.

We believe these advantages make the FDTD method an attractive alternative to e.g. the more widespread finite-difference frequency-domain method. For example, given a machine with a specific amount of memory, the FDTD method will always be able to handle problems with significantly more electromagnetic field unknowns than its frequency-domain counterpart.

A design criterion for vertical node spacing has been obtained based on dispersion analysis. It shows that the vertical node spacing can be gradually increased as a function of depth for the case of a half-space. This may prove to be a useful starting point to design grids for

finite-difference MT modeling. This criterion can also be used with finite-difference frequency-domain schemes.

ACKNOWLEDGMENTS

The authors wish to thank EMGS for permission to publish the results and D. Shantsev for numerous interesting discussions. They also wish to thank Xavier Garcia, Sofia Davydycheva, and two anonymous reviewers for constructive comments that helped significantly improve the manuscript.

APPENDIX A

DIFFUSIVE GREEN'S TENSORS

Expressions for $\mathcal{G}^{E,H|J,K}$ as a function of $\mathcal{G}'^{E,H|J,K}$ have previously been established (de Hoop [1996], equation 24). The parameter α from de Hoop (1996) corresponds to our parameter ω_0 from equation 8, with $\alpha = 2\omega_0$. To obtain a relation between $\mathbf{G}^{E,H|J,K}(\mathbf{x}, \omega|\tilde{\mathbf{x}})$ and $\mathcal{G}'^{E,H|J,K}(\mathbf{x}, t'|\tilde{\mathbf{x}})$, it hence suffices to take a Fourier transform. For example, for $\mathbf{G}^{E|K}$ we have

$$\begin{aligned} \mathbf{G}^{E|K}(\mathbf{x}, \omega|\tilde{\mathbf{x}}) &= \int_{t=0}^{\infty} \mathcal{G}^{E|K}(\mathbf{x}, t|\tilde{\mathbf{x}}) e^{i\omega t} dt \\ &= \int_{t=0}^{\infty} \left[\int_{t'=0}^{\infty} \mathcal{G}'^{E|K}(\mathbf{x}, t'|\tilde{\mathbf{x}}) \sqrt{\frac{\omega_0}{2\pi}} \frac{t' e^{-\frac{\omega_0 t'^2}{2t}}}{t^{3/2}} dt' \right] e^{i\omega t} dt \\ &= \sqrt{\frac{\omega_0}{2\pi}} \int_{t'=0}^{\infty} \mathcal{G}'^{E|K}(\mathbf{x}, t'|\tilde{\mathbf{x}}) \left[\int_{t=0}^{\infty} e^{i\omega t} \frac{t' e^{-\frac{\omega_0 t'^2}{2t}}}{t^{3/2}} dt \right] dt' \\ &= \int_{t'=0}^{\infty} \mathcal{G}'^{E|K}(\mathbf{x}, t'|\tilde{\mathbf{x}}) e^{-\sqrt{\omega\omega_0}t'} e^{i\sqrt{\omega\omega_0}t'} dt'. \quad (\text{A-1}) \end{aligned}$$

Here, the second equality in the chain follows directly from equation 24 in de Hoop (1996); the third equality follows by interchanging the order of integration, which is legitimate because the integrand is continuous over $(t, t') \in (0, \infty) \times (0, \infty)$; and the fourth equality follows by applying formula 29.3.82 from Abramowitz and Stegun (1972) with $s = -i\omega$ and $k = \sqrt{2\omega_0}t'$. We can formally show that the integral

$$\int_{t=0}^{\infty} e^{i\omega t} \frac{t' e^{-\frac{\omega_0 t'^2}{2t}}}{t^{3/2}} dt \quad (\text{A-2})$$

converges, and hence that formula 29.3.82 from Abramowitz and Stegun (1972) is valid for $s = -i\omega$, by applying theorem 13.95 from Titchmarsh (1939). The only requirement is that

$$\int_{t=0}^{\infty} \left(\frac{1}{t^{3/2}} e^{-\frac{\omega_0 t'^2}{2t}} \right)^2 dt < \infty, \quad (\text{A-3})$$

which is seen by first making the variable transformation $t = 1/\tilde{t}$ and then using formula 2.322 from Gradshteyn and Ryzhik (2007) to evaluate the integral.

Similarly, for $\mathbf{G}^{E|J}$, we obtain

$$\begin{aligned} \mathbf{G}^{E|J}(\mathbf{x}, \omega|\tilde{\mathbf{x}}) &= \int_{t=0}^{\infty} \mathcal{G}^{E|J}(\mathbf{x}, t|\tilde{\mathbf{x}}) e^{i\omega t} dt \\ &= \int_{t=0}^{\infty} \left[\int_{t'=0}^{\infty} \mathcal{G}'^{E|J}(\mathbf{x}, t'|\tilde{\mathbf{x}}) \frac{-1}{2\omega_0} \frac{\partial}{\partial t'} \left\{ \sqrt{\frac{\omega_0}{2\pi}} \frac{t' e^{-\frac{\omega_0 t'^2}{2t}}}{t^{3/2}} \right\} dt' \right] e^{i\omega t} dt \\ &= \frac{-1}{2\omega_0} \int_{t'=0}^{\infty} \mathcal{G}'^{E|J}(\mathbf{x}, t'|\tilde{\mathbf{x}}) \left[\int_{t=0}^{\infty} \frac{\partial}{\partial t'} \left\{ \sqrt{\frac{\omega_0}{2\pi}} e^{i\omega t} \frac{t' e^{-\frac{\omega_0 t'^2}{2t}}}{t^{3/2}} \right\} dt \right] dt' \\ &= \frac{-1}{2\omega_0} \int_{t'=0}^{\infty} \mathcal{G}'^{E|J}(\mathbf{x}, t'|\tilde{\mathbf{x}}) \left[\frac{\partial}{\partial t'} \int_{t=0}^{\infty} \sqrt{\frac{\omega_0}{2\pi}} e^{i\omega t} \frac{t' e^{-\frac{\omega_0 t'^2}{2t}}}{t^{3/2}} dt \right] dt' \\ &= \sqrt{\frac{-i\omega}{2\omega_0}} \int_{t'=0}^{\infty} \mathcal{G}'^{E|J}(\mathbf{x}, t'|\tilde{\mathbf{x}}) e^{-\sqrt{\omega\omega_0}t'} e^{i\sqrt{\omega\omega_0}t'} dt', \quad (\text{A-4}) \end{aligned}$$

where the second equality in the chain again follows from equation 24 in de Hoop (1996); the third equality follows by interchanging the order of integration, which is legitimate because the integrand is continuous over $(t, t') \in (0, \infty) \times (0, \infty)$; the exchange of the order of differentiation and integration in the fourth equality follows by virtue of Lebesgue's dominated convergence theorem; and the last equality is obtained by evaluating the integral over t with formula 29.3.82 from Abramowitz and Stegun (1972) as in the case of $\mathbf{G}^{E|K}$ discussed above.

Expressions for $\mathbf{G}^{H|J}$ and $\mathbf{G}^{H|K}$ as a function of, respectively, $\mathcal{G}'^{H|J}$ and $\mathcal{G}'^{H|K}$ can be obtained using the same procedure. This gives

$$\mathbf{G}^{H|J}(\mathbf{x}, \omega|\tilde{\mathbf{x}}) = \int_{t'=0}^{\infty} \mathcal{G}'^{H|J}(\mathbf{x}, t'|\tilde{\mathbf{x}}) e^{-\sqrt{\omega\omega_0}t'} e^{i\sqrt{\omega\omega_0}t'} dt' \quad (\text{A-5})$$

and

$$\mathbf{G}^{H|K}(\mathbf{x}, \omega|\tilde{\mathbf{x}}) = \sqrt{\frac{-2\omega_0}{i\omega}} \int_{t'=0}^{\infty} \mathcal{G}'^{H|K}(\mathbf{x}, t'|\tilde{\mathbf{x}}) e^{-\sqrt{\omega\omega_0}t'} e^{i\sqrt{\omega\omega_0}t'} dt'. \quad (\text{A-6})$$

APPENDIX B

CPML VARIABLE PROFILES

In this section, we specify our choices for quantity e'_ξ and the functions $\alpha_\xi(u) \geq 1$, $\sigma_\xi(u) \geq 0$, and $\tau_\xi(u) \geq 0$, all of which influence the performance of the CPML ABCs we use in our FDTD MT modeling scheme (see equation 11). Our choices are based on ideas from Rickard and Georgieva (2003) and Taflove and Hagness (2005). We set

$$\sigma_\xi(u) = \sigma_{\max, \xi} \left(\frac{u}{\delta_\xi} \right)^{n+\beta}, \quad (\text{B-1})$$

$$\alpha_\xi(u) = 1 + \gamma_{\max, \xi} \left(\frac{u}{\delta_\xi} \right)^n, \quad (\text{B-2})$$

where δ_ξ is the CPML thickness in direction $\xi \in \{x, y, z\}$; $0 \leq u \leq \delta_\xi$ is the depth in the CPML; n and β are such that $n > 1$ and $(n + \beta) > 1$; $\gamma_{\max, \xi} > 0$ controls the rate of evanescent mode attenuation; and $\sigma_{\max, \xi}$, controlling the rate of attenuation of propagating waves, has the form

$$\sigma_{\max,\xi} = -\frac{(n + \beta + 1) \cdot \log R_0}{2\delta_\xi \cdot \sqrt{\epsilon'_\xi \mu_0}}. \quad (\text{B-3})$$

Here, R_0 , the reflection coefficient at normal incidence, is to be defined by the user, and ϵ'_ξ is a suitable average of ϵ' . We choose

$$\epsilon'_\xi = \frac{1}{2} \left[|\mathcal{P}_\eta|^{-1} \sum_{\mathbf{x} \in \mathcal{P}_\eta} \epsilon'_{\eta\eta}(\mathbf{x}) + |\mathcal{P}_\nu|^{-1} \sum_{\mathbf{x} \in \mathcal{P}_\nu} \epsilon'_{\nu\nu}(\mathbf{x}) \right] \quad (\text{B-4})$$

with η and ν chosen such that (ξ, η, ν) is a permutation of (x, y, z) , $\mathcal{P}_\eta \subset \Omega'_N$ the plane of \mathcal{E}'_η nodes immediately before the start of the relevant CPML in direction ξ , and a similar definition for \mathcal{P}_ν .

We note that in the special case in which $\sigma_\xi(u) = \tau_\xi(u) = 0$, we have $s_\xi(u, \omega') = \alpha_\xi(u)$, which corresponds to purely real coordinate stretching. It is reasonable to conjecture that in the case of a large cell size $\Delta\xi$ in direction ξ , less stretching in direction ξ would be required to obtain good CPML absorption properties than in the case of small $\Delta\xi$. We hence set

$$\gamma_{\max,\xi} = \frac{k}{\Delta\xi}, \quad (\text{B-5})$$

where k is a user-defined parameter.

Finally, our choice for $\tau_\xi(u)$ is

$$\tau_\xi(u) = \frac{\tau_{\max}}{\epsilon'_\xi} \left(1 - \frac{u}{\delta_\xi} \right), \quad (\text{B-6})$$

where ϵ'_ξ is defined in equation B-4, and $\tau_{\max} > 0$ is a user-defined parameter.

To summarize, we see the above CPML variable profiles depend on the parameters $S = \{n, \beta, R_0, k, \tau_{\max}\}$. Our primary concern in an MT modeling setting is that for a given choice of these parameters and a given CPML thickness, the resulting absorption properties be as good as possible for all frequencies and earth background conductivities $\sigma = 2\omega_0\epsilon'$ one may wish to compute MT responses for.

We performed a search over approximately 3.5×10^5 different sets S and found, for example, that 10-cell-thick CPMLs with the parameter combination

$$S_1 = \{2, 1.5, 10^{-6}, 50, 10^{-3}\} \quad (\text{B-7})$$

had extremely good absorption properties and were suitable for MT modeling.

APPENDIX C

HIGH-ORDER SPATIAL DIFFERENTIATION AND COORDINATE TRANSFORMATION

Our FDTD MT modeling scheme can be used in combination with high-order spatial differential operators and the coordinate transformation method described by [Fornberg \(1988\)](#). We discuss this here.

The high-order spatial scheme is discussed in detail in [Mittet \(2010\)](#). However, there are two points not covered there that are relevant for this MT modeling scheme. The first issue is related to the implementation of the direct downgoing MT source field with the increased number of ghost nodes that follows from increased

operator lengths. The second is related to coordinate stretching in combination with high-order difference operators.

As a consequence of longer spatial operators, we will have electric and magnetic ghost nodes above the air-water interface. Thus, we will have to give source-field values to electric and magnetic field components above the air-water interface. We use the following reasoning: The low-frequency downgoing electric and magnetic source fields in the air layer will vary slowly with depth due to the high propagation velocity. Thus, for a plane downgoing wave at a given time step, we set the magnetic field to the same value for all levels above the air-water interface. The reflection coefficient for the electric field at the air-water interface is very close to minus unity. The resulting effect is a destructive interference in the air layer immediately above the air-water interface. Thus, for the downgoing source-field, we set the values of the horizontal components of the electric field to zero at the ghost nodes. Note also that the transmission coefficient from air to water for a downgoing electric field is zero; thus, we are not very sensitive to the actual value of the electric field in the air layer. We enforce the previously described zero-derivative condition for the fields at the vertical boundaries of the grid.

Coordinate stretching can be formalized by the coordinate transformation method described by [Fornberg \(1988\)](#). Fornberg discusses a method in which the grid for discretizing the real world can be general, even with local curvature. He then describes the transform that goes from this general grid to a regular grid with fixed step lengths. The transformation method is valid for spatial schemes of any order, pseudospectral schemes included.

The method is considerably simplified if the real world coordinate axes are mutually orthogonal. In this case, each axis can be treated separately. As an example, we discuss the z -axis here. Assume that the real-world depth is described by a stretched grid, which will not be the simulation grid, on the z -axis. We introduce a new depth coordinate η with a regular grid for use in the finite-difference simulations. The relations between these two coordinates are given by the transform functions $T(z)$ and $S(\eta)$ such that $\eta(z) = S(z)$ and $z(\eta) = T(\eta)$. We introduce $\partial_\eta T(\eta) = \tau(\eta)^{-1}$ such that, e.g., a z -derivative of the x -component of the electric field $\mathcal{E}'_x(x, y, z, t')$ takes the form

$$\partial_z \mathcal{E}'_x(x, y, z, t') = \tau(\eta) \partial_\eta \mathcal{E}'_x(x, y, \eta, t'). \quad (\text{C-1})$$

Care must be taken when the transform functions are defined. The function $T(\eta)$ must be such that τ is positive to have a stable finite-difference scheme, and, as discussed previously, gradual stretching as a function of depth is to be preferred to suppress numerical artifacts. The grid stretching on the z -axis can be interpreted on the regular η grid as a modification of the propagation velocity. If this effect is properly treated, we note that the dispersion and stability analysis for the scheme on the regular grid can be performed in the same way as described by [Mittet \(2010\)](#) without any further assumptions.

APPENDIX D

NUMERICAL DISPERSION AND VERTICAL SPACING REQUIREMENTS

Let us consider a 1D earth model consisting of an isotropic half-space with conductivity $\sigma = 2\omega_0\epsilon'$ in the region $z \geq 0$. Let us assume that Yee's FDTD scheme in the fictitious-wave domain

is used to compute electromagnetic fields. The boundary condition $\mathcal{E}'_x(z = 0, t') = f(t')$, with $f(t') = 0$ for $t' < 0$, is imposed on the plane $z = 0$. There is no other source of excitation to the system. In this appendix, we first show how to evaluate the numerical dispersion associated with our fictitious-wave domain FDTD scheme in such a scenario. This is done by showing that we can use analytic continuation to extend well-known results for the case in which $\omega' \in \mathbb{R}$ to complex values of ω' . We then use this result to determine requirements for the FDTD grid vertical spacing Δz as a function of depth in order for dispersion to be low.

Numerical dispersion

Because with the above assumptions none of the quantities appearing in equations 6 and 7 depend on the spatial coordinates x or y , the functional dependence with regard to these variables is omitted throughout this appendix. Moreover, because the system is excited by a causal signal $f(t')$, all time-dependent quantities appearing in equations 6 and 7 are identically zero for $t' < 0$.

For any $z > 0$, let $\mathcal{E}'_x(z, t')$ denote the x -oriented electric field that would be computed by an ideal, dispersionless fictitious-wave domain FDTD algorithm. It can be calculated using an exact analytical expression. Let $\mathcal{E}'_{x,\text{FDTD}}(z, t')$ denote the corresponding quantity computed by a fictitious-wave domain FDTD algorithm with dispersion.

The Fourier transform of $\mathcal{E}'_x(z, t')$ is defined for $z \geq 0$ and $\omega' \in \mathbb{R}$ as

$$E'_x(z, \omega') = \int_0^\infty \mathcal{E}'_x(z, t') e^{i\omega' t'} dt'. \quad (\text{D-1})$$

By virtue of Titchmarsh's theorem (Titchmarsh [1948], theorem 95), one can use analytic continuation to extend the domain of $E'_x(z, \omega')$ from $\omega' \in \mathbb{R}$ to all $\omega' \in \mathbb{C}$ such that $\text{Im } \omega' \geq 0$. This analytic continuation is unique and is given by (Titchmarsh [1948], chapter 5)

$$E'_x(z, \omega') = \int_0^\infty \mathcal{E}'_x(z, t') e^{i\nu_a t'} e^{-\nu_b t'} dt', \quad (\text{D-2})$$

with $\omega' = \nu_a + i\nu_b$ ($\nu_a \in \mathbb{R}; \nu_b \in \mathbb{R}^+$). Note that setting $\nu_a = \nu_b = \sqrt{\omega\omega_0}$ in equation D-2 above allows us to recover the quantity $E_x(\omega)$ defined in equation 10; i.e., $E'_x(z, (1+i)\sqrt{\omega\omega_0}) = E_x(z, \omega)$.

Similarly, it is possible to define the Fourier transform $E'_{x,\text{FDTD}}(z, \omega')$ of $\mathcal{E}'_{x,\text{FDTD}}(z, t')$ for $z \geq 0$ and $\omega' \in \mathbb{R}$, and again extend this definition to all $\omega' \in \mathbb{C}$ such that $\text{Im } \omega' \geq 0$ by analytic continuation. As before, setting $\mathcal{E}'_x(\mathbf{x}, t') = \mathcal{E}'_{x,\text{FDTD}}(z, t')$ in equation 10, we see that

$$E'_{x,\text{FDTD}}(z, (1+i)\sqrt{\omega\omega_0}) = E_{x,\text{FDTD}}(z, \omega). \quad (\text{D-3})$$

Now, for any $z > 0$, let $g(z, \omega')$ be such that

$$E'_{x,\text{FDTD}}(z, \omega') = g(z, \omega') E'_x(z, \omega') \quad (\text{D-4})$$

for all $\omega' \in \mathbb{R}$. Let us assume that the domain of $g(z, \omega')$ can be extended by analytic continuation from $\omega' \in \mathbb{R}$ to all $\omega' \in \mathcal{D} \subseteq \mathbb{C}$ such that $\text{Im } \omega' \geq 0$, with \mathcal{D} being an open subset of \mathbb{C} . (At the end of this appendix, we characterize $g(z, \omega')$ and \mathcal{D} more closely for the special case of Yee's FDTD scheme with uniform spacing

Δz in the z -direction applied to the 1D model and excitation described above.) Hence, the function $g(z, \omega') E'_x(z, \omega')$ is analytic for all $\omega' \in \mathcal{D}$ such that $\text{Im } \omega' \geq 0$, and because

$$\lim_{\nu_b \rightarrow 0} g(z, \omega') E'_x(z, \omega') = E'_{x,\text{FDTD}}(z, \omega'), \quad (\text{D-5})$$

$g(z, \omega') E'_x(z, \omega')$ must also be equal, for all $\omega' \in \mathcal{D}$ such that $\text{Im } \omega' \geq 0$, to the function $E'_{x,\text{FDTD}}(z, \omega')$ already obtained above by analytic continuation. This is because the analytic continuation of the function $E'_{x,\text{FDTD}}(z, \omega')$ from $\omega' \in \mathbb{R}$ to all $\omega' \in \mathbb{C}$ such that $\text{Im } \omega' \geq 0$ is unique. Finally, for any ω such that $(1+i)\sqrt{\omega\omega_0} \in \mathcal{D}$, we see that using our fictitious-wave domain Yee FDTD scheme to compute $E_{x,\text{FDTD}}(z, \omega)$ based on equation 10 leads to a dispersion error

$$g(z, (1+i)\sqrt{\omega\omega_0}) = \frac{E_{x,\text{FDTD}}(z, \omega)}{E_x(z, \omega)}. \quad (\text{D-6})$$

Let us now examine $g(z, \omega')$ and \mathcal{D} more closely for the special case of Yee's FDTD scheme with uniform spacing Δz in the z -direction applied to the 1D model and excitation described at the beginning of this appendix. For an angular frequency $\omega' \in \mathbb{R}$, the exact wavenumber is $k_z = \omega' \sqrt{\epsilon' \mu_0}$, whereas the corresponding wavenumber \tilde{k}_z obtained upon discretization using Yee's FDTD scheme with grid spacing Δz in the z -direction and time step $\Delta t'$ obeys the relation (Taflove and Hagness, 2005)

$$\frac{\sin(\tilde{k}_z \Delta z / 2)}{\Delta z} = \frac{\sin(\omega' \Delta t' / 2)}{\Delta t'} \sqrt{\epsilon' \mu_0}. \quad (\text{D-7})$$

Let

$$\tilde{k}_z = \frac{2}{\Delta z} \arcsin \left[\frac{\Delta z \sqrt{\epsilon' \mu_0}}{\Delta t'} \times \sin(\omega' \Delta t' / 2) \right]. \quad (\text{D-8})$$

After propagation over a distance z , we have for $\omega' \in \mathbb{R}$,

$$g(z, \omega') = \frac{E'_{x,\text{FDTD}}(z, \omega')}{E'_x(z, \omega')} = e^{i(\tilde{k}_z(\omega') - k_z(\omega'))z}. \quad (\text{D-9})$$

Now, the functions $\exp(i\omega')$, $\omega' \sqrt{\epsilon' \mu_0}$, and $\sin(\omega' \Delta t' / 2)$ of the real variable ω' can be extended by analytic continuation to the entire complex plane. The principal value of the complex arcsin function is analytic over the entire complex plane, except for the intervals $(-\infty, -1]$ and $[1, \infty)$, where it has branch cuts. The domain of the function $\tilde{k}_z(\omega')$ defined in equation D-8, and as a consequence also that of $g(z, \omega')$, can hence be extended by analytic continuation to the entire complex plane, except possibly for the intervals $(\frac{(2n+1)\pi}{\Delta t'} - i\infty, \frac{(2n+1)\pi}{\Delta t'} - i\nu_{b_n}]$ and $(\frac{(2n+1)\pi}{\Delta t'} + i\nu_{b_n}, \frac{(2n+1)\pi}{\Delta t'} + i\infty)$, where there are branch cuts. Here, $n \in \{0, 1, 2, \dots\}$ and $\nu_{b_n} > 0$ is a constant that depends on the values $\Delta t'$, Δz , and $\sqrt{\epsilon' \mu_0}$.

Vertical spacing requirements

Let us now consider a receiver located at $z = z_0$ measuring $E_x(z, \omega_a)$ for real-world angular frequency ω_a in a scenario with

a perfect electromagnetic reflector at depth $z = z_0 + m\delta(\omega_a)$ inside the half-space with conductivity σ . Here, $\delta(\omega_a)$ is the skin depth at angular frequency ω_a inside this half-space and m is a constant discussed further below. Let the constant $\gamma > 0$ denote a dispersion error level deemed acceptable for $E_x(z, \omega_a)$, in the sense that

$$1 - \gamma \leq \left| g\left(z, (1+i)\sqrt{\omega_a\omega_0}\right) \right| \leq 1 + \gamma, \quad (\text{D-10})$$

$$\left| \arg g\left(z, (1+i)\sqrt{\omega_a\omega_0}\right) \right| \leq \gamma. \quad (\text{D-11})$$

The receiver located at $z = z_0$ will see a first arrival resulting from the plane-wave excitation at $z = 0$ directly propagating to $z = z_0$, and a later arrival corresponding to an event in which the plane-wave source penetrates m skin depths beyond z_0 , undergoes reflection at depth $z = z_0 + m\delta(\omega_a)$, and then travels m skin depths back to $z = z_0$. In order for the value of $E_x(z_0, \omega_a)$ to depend not only on the first arrival but also on the later arrival, m cannot be significantly greater than two. It is hence reasonable to require that conditions D-10 and D-11 hold for a propagation distance z of up to $2m = 4$ skin depths $\delta(\omega_a)$.

The expression for g from equation D-9 can be used to determine requirements for the spacing Δz as a function of depth such that conditions D-10 and D-11 hold for all $z \leq 2m\delta(\omega_a)$ without making any approximations. However, the case in which $|\omega'\Delta t'| \ll 1$ and $|\tilde{k}_z(\omega')\Delta z| \ll 1$ for $\omega' = (1+i)\sqrt{\omega\omega_0}$ in equation D-9 is of particular interest because the numerical dispersion will be small (e.g., $\gamma < 1\%$). In this case, a simplification is possible by performing a series expansion of the expression,

$$[\tilde{k}_z(\omega') - k_z(\omega')]z = k_z(\omega')z[\tilde{k}_z(\omega')/k_z(\omega') - 1], \quad (\text{D-12})$$

which appears in equation D-9. This gives, keeping only the lowest order terms in $\omega'\Delta t'$ and $\tilde{k}_z(\omega')\Delta z$,

$$\frac{\tilde{k}_z(\omega')}{k_z(\omega')} - 1 \approx \frac{1}{24}(\tilde{k}_z(\omega')\Delta z)^2 \left(1 - \left(\frac{c_\sigma \Delta t'}{\Delta z} \right)^2 \right), \quad (\text{D-13})$$

where $c_\sigma = \sqrt{2\omega_0/\mu\sigma}$ is the propagation velocity through the half-space with conductivity σ . This in turn leads to

$$g(z, (1+i)\sqrt{\omega\omega_0}) \approx e^{-\frac{z\Delta z^2}{12\delta^3(\omega)} \left[1 - \left(\frac{c_\sigma \Delta t'}{\Delta z} \right)^2 \right]} e^{-i\frac{z\Delta z^2}{12\delta^3(\omega)} \left[1 - \left(\frac{c_\sigma \Delta t'}{\Delta z} \right)^2 \right]} \quad (\text{D-14})$$

and

$$\left| g(z, (1+i)\sqrt{\omega\omega_0}) \right| \approx 1 - \frac{z\Delta z^2}{12\delta^3(\omega)} \left[1 - \left(\frac{c_\sigma \Delta t'}{\Delta z} \right)^2 \right], \quad (\text{D-15})$$

with $\delta(\omega)$ being the skin depth at angular frequency ω in the half-space with conductivity σ .

In general, referring to equations D-14 and D-15, we see that conditions D-14 and D-15 approximately hold for all $z \leq 2m\delta(\omega_a)$ if

$$\Delta z < \sqrt{\frac{6\gamma}{m} \delta^2(\omega_a) + (c_\sigma \Delta t')^2}. \quad (\text{D-16})$$

Note that $c_\sigma \Delta t'$ will be independent of ω_0 if $\Delta t'$ is chosen based on stability criterion 14. Clearly, as ω_a decreases, $\delta(\omega_a)$ increases, the interval $z_0 \leq z \leq z_0 + m\delta(\omega_a)$ over which condition 15 or 16 must hold becomes larger, but so does the maximum allowed vertical spacing Δz . We hence see that Δz can be gradually increased as a function of depth.

APPENDIX E

ADJOINT STATE SOURCES

The adjoint state electric and magnetic dipole sources depend on the impedance misfits and the predicted fields at the receiver locations. The iteration index n is omitted in the following. Let $\Delta B_{ij}(\mathbf{x}_r, \omega)$ be defined as

$$\Delta B_{ij}(\mathbf{x}_r, \omega) = W_{ij}(\mathbf{x}_r, \omega) \frac{\Delta Z_{ij}(\mathbf{x}_r, \omega)}{H_{\det}(\mathbf{x}_r, \omega)}, \quad (\text{E-1})$$

with

$$H_{\det}(\mathbf{x}_r, \omega) = H_{xx}(\mathbf{x}_r, \omega)H_{yy}(\mathbf{x}_r, \omega) - H_{xy}(\mathbf{x}_r, \omega)H_{yx}(\mathbf{x}_r, \omega), \quad (\text{E-2})$$

where for receiver \mathbf{x}_r and angular frequency ω , $H_{ij}(\mathbf{x}_r, \omega)$ denotes the i -component of the predicted magnetic field due to a j -polarized MT source. The electric source contributions to the adjoint state are then

$$\begin{aligned} \Delta J_{xx}(\mathbf{x}_r, \omega) &= \Delta B_{xx}(\mathbf{x}_r, \omega)H_{yy}(\mathbf{x}_r, \omega) \\ &\quad - \Delta B_{xy}(\mathbf{x}_r, \omega)H_{xy}(\mathbf{x}_r, \omega), \\ \Delta J_{yx}(\mathbf{x}_r, \omega) &= \Delta B_{yx}(\mathbf{x}_r, \omega)H_{yy}(\mathbf{x}_r, \omega) \\ &\quad - \Delta B_{yy}(\mathbf{x}_r, \omega)H_{xy}(\mathbf{x}_r, \omega), \\ \Delta J_{xy}(\mathbf{x}_r, \omega) &= \Delta B_{xy}(\mathbf{x}_r, \omega)H_{xx}(\mathbf{x}_r, \omega) \\ &\quad - \Delta B_{xx}(\mathbf{x}_r, \omega)H_{yx}(\mathbf{x}_r, \omega), \\ \Delta J_{yy}(\mathbf{x}_r, \omega) &= \Delta B_{yy}(\mathbf{x}_r, \omega)H_{xx}(\mathbf{x}_r, \omega) \\ &\quad - \Delta B_{yx}(\mathbf{x}_r, \omega)H_{yx}(\mathbf{x}_r, \omega), \end{aligned} \quad (\text{E-3})$$

and the magnetic source contributions are

$$\begin{aligned}
\Delta K_{xx}(\mathbf{x}_r, \omega) &= \Delta B_{xx}(\mathbf{x}_r, \omega) Z_{xx}(\mathbf{x}_r, \omega) H_{yy}(\mathbf{x}_r, \omega) \\
&\quad + \Delta B_{yx}(\mathbf{x}_r, \omega) Z_{yx}(\mathbf{x}_r, \omega) H_{yy}(\mathbf{x}_r, \omega) \\
&\quad - \Delta B_{xy}(\mathbf{x}_r, \omega) [E_{xy}(\mathbf{x}_r, \omega) - Z_{xy}(\mathbf{x}_r, \omega) H_{yy}(\mathbf{x}_r, \omega)] \\
&\quad - \Delta B_{yy}(\mathbf{x}_r, \omega) [E_{yy}(\mathbf{x}_r, \omega) - Z_{yy}(\mathbf{x}_r, \omega) H_{yy}(\mathbf{x}_r, \omega)], \\
\Delta K_{yx}(\mathbf{x}_r, \omega) &= \Delta B_{xx}(\mathbf{x}_r, \omega) [E_{xy}(\mathbf{x}_r, \omega) - Z_{xx}(\mathbf{x}_r, \omega) H_{xy}(\mathbf{x}_r, \omega)] \\
&\quad + \Delta B_{yx}(\mathbf{x}_r, \omega) [E_{yy}(\mathbf{x}_r, \omega) - Z_{yx}(\mathbf{x}_r, \omega) H_{xy}(\mathbf{x}_r, \omega)] \\
&\quad - \Delta B_{xy}(\mathbf{x}_r, \omega) Z_{yx}(\mathbf{x}_r, \omega) H_{xy}(\mathbf{x}_r, \omega) \\
&\quad - \Delta B_{yy}(\mathbf{x}_r, \omega) Z_{yy}(\mathbf{x}_r, \omega) H_{xy}(\mathbf{x}_r, \omega), \\
\Delta K_{xy}(\mathbf{x}_r, \omega) &= -\Delta B_{xx}(\mathbf{x}_r, \omega) Z_{xx}(\mathbf{x}_r, \omega) H_{yx}(\mathbf{x}_r, \omega) \\
&\quad - \Delta B_{yx}(\mathbf{x}_r, \omega) Z_{yx}(\mathbf{x}_r, \omega) H_{yx}(\mathbf{x}_r, \omega) \\
&\quad + \Delta B_{xy}(\mathbf{x}_r, \omega) [E_{xx}(\mathbf{x}_r, \omega) - Z_{xy}(\mathbf{x}_r, \omega) H_{yx}(\mathbf{x}_r, \omega)] \\
&\quad + \Delta B_{yy}(\mathbf{x}_r, \omega) [E_{yx}(\mathbf{x}_r, \omega) - Z_{yy}(\mathbf{x}_r, \omega) H_{yx}(\mathbf{x}_r, \omega)], \\
\Delta K_{yy}(\mathbf{x}_r, \omega) &= -\Delta B_{xx}(\mathbf{x}_r, \omega) [E_{xx}(\mathbf{x}_r, \omega) - Z_{xx}(\mathbf{x}_r, \omega) H_{xx}(\mathbf{x}_r, \omega)] \\
&\quad - \Delta B_{yx}(\mathbf{x}_r, \omega) [E_{yx}(\mathbf{x}_r, \omega) - Z_{yx}(\mathbf{x}_r, \omega) H_{xx}(\mathbf{x}_r, \omega)] \\
&\quad + \Delta B_{xy}(\mathbf{x}_r, \omega) Z_{yx}(\mathbf{x}_r, \omega) H_{xx}(\mathbf{x}_r, \omega) \\
&\quad + \Delta B_{yy}(\mathbf{x}_r, \omega) Z_{yy}(\mathbf{x}_r, \omega) H_{xx}(\mathbf{x}_r, \omega). \quad (\text{E-4})
\end{aligned}$$

The complex conjugates of the above electric and magnetic dipole source functions are used in equations 25 and 26 for the estimation of the time-domain sources.

REFERENCES

- Abramowitz, M., and I. Stegun, 1972, Handbook of mathematical functions, 10th ed.: National Bureau of Standards.
- Avdeev, D. B., 2005, Three-dimensional electromagnetic modelling and inversion from theory to application: Surveys in Geophysics, **26**, 767–799, doi: [10.1007/s10712-005-1836-x](https://doi.org/10.1007/s10712-005-1836-x).
- Avdeeva, A., D. Avdeev, and M. Jegen, 2012, Detecting a salt dome overhang with magnetotellurics: 3D inversion methodology and synthetic model studies: Geophysics, **77**, no. 4, E251–E263, doi: [10.1190/geo2011-0167.1](https://doi.org/10.1190/geo2011-0167.1).
- Börner, R., 2010, Numerical modelling in geo-electromagnetics: Advances and challenges: Surveys in Geophysics, **31**, 225–245, doi: [10.1007/s10712-009-9087-x](https://doi.org/10.1007/s10712-009-9087-x).
- Byrd, R. H., P. Lu, and J. Nocedal, 1995, A limited memory algorithm for bound constrained optimization: SIAM Journal on Scientific and Statistical Computing, **16**, 1190–1208, doi: [10.1137/0916069](https://doi.org/10.1137/0916069).
- Carcione, J. M., 2006, A spectral numerical method for electromagnetic diffusion: Geophysics, **71**, no. 1, 11–19, doi: [10.1190/1.2159050](https://doi.org/10.1190/1.2159050).
- Cessenat, O., 2013, Sophie, an FDTD code on the way to multicore, getting rid of the memory bandwidth bottleneck better using cache: arXiv:1301.4539.
- Chew, W. C., and W. H. Weedon, 1994, A 3D perfectly matched medium from modified Maxwell's equations with stretched coordinates: Microwave and Optical Technology Letters, **7**, 599–604, doi: [10.1002/mop.4650071304](https://doi.org/10.1002/mop.4650071304).
- Constable, S. C., A. Orange, G. M. Hovertsen, and H. F. Morrison, 1998, Marine magnetotellurics for petroleum exploration, Part I: A sea-floor equipment system: Geophysics, **63**, 816–825, doi: [10.1190/1.1444393](https://doi.org/10.1190/1.1444393).
- De Groot-Hedlin, C., 2006, Finite-difference modeling of magnetotelluric fields: Error estimates for uniform and nonuniform grids: Geophysics, **71**, no. 3, G97–G106, doi: [10.1190/1.2195991](https://doi.org/10.1190/1.2195991).
- De Hoop, A. T., 1996, A general correspondence principle for time-domain electromagnetic wave and diffusion fields: Geophysical Journal International, **127**, 757–761, doi: [10.1111/j.1365-246X.1996.tb04054.x](https://doi.org/10.1111/j.1365-246X.1996.tb04054.x).
- Druskin, V., and L. Knizhnerman, 1988, Spectral differential-difference method for numeric solution of three-dimensional nonstationary problems of electric prospecting: Izvestiya, Solid Earth Physics, **24**, 641–648.
- Druskin, V., and L. Knizhnerman, 1994, Spectral approach to solving Maxwell's diffusion equations in the time and frequency domains: Radio Science, **29**, 937–953, doi: [10.1029/94RS00747](https://doi.org/10.1029/94RS00747).
- Edelvik, F., R. Schuhmann, and T. Weiland, 2004, A general stability analysis of FIT/FDTD applied to lossy dielectrics and lumped elements: International Journal of Numerical Modelling, **17**, 407–419, doi: [10.1002/jnm.547](https://doi.org/10.1002/jnm.547).
- Farquharson, C. G., and M. P. Miensopust, 2011, Three-dimensional finite-element modelling of magnetotelluric data with a divergence correction: Journal of Applied Geophysics, **75**, 699–710, doi: [10.1016/j.jappgeo.2011.09.025](https://doi.org/10.1016/j.jappgeo.2011.09.025).
- Farquharson, C. G., and D. W. Oldenburg, 2002, An algorithm for three-dimensional inversion of magnetotelluric data: 72nd Annual International Meeting, SEG, Expanded Abstracts, 649–652.
- Fornberg, B., 1988, The pseudospectral method: Accurate representation of interfaces in elastic calculations: Geophysics, **53**, 625–637, doi: [10.1190/1.1442497](https://doi.org/10.1190/1.1442497).
- Gradshteyn, I., and I. Ryzhik, 2007, Table of integrals, series, and products, 7th ed.: Elsevier.
- Hovertsen, G. M., H. F. Morrison, and S. C. Constable, 1998, Marine magnetotellurics for petroleum exploration, Part II: Numerical analysis of subsalt resolution: Geophysics, **63**, 826–840, doi: [10.1190/1.1444394](https://doi.org/10.1190/1.1444394).
- Hursan, G., and M. S. Zhdanov, 2002, Contraction integral equation method in three-dimensional electromagnetic modeling: Radio Science, **37**, 1089, doi: [10.1029/2001RS002513](https://doi.org/10.1029/2001RS002513).
- Key, K., 2003, Application of broadband marine magnetotelluric exploration to a 3D salt structure and a fast-spreading ridge: Ph.D. thesis, University of California.
- Key, K., 2012, Marine electromagnetic studies of seafloor resources and tectonics: Surveys in Geophysics, **33**, 135–167, doi: [10.1007/s10712-011-9139-x](https://doi.org/10.1007/s10712-011-9139-x).
- Key, K., S. C. Constable, and C. Weiss, 2006, Mapping 3D salt using the 2D marine magnetotelluric method: Case study from the Gemini Prospect, Gulf of Mexico: Geophysics, **71**, no. 1, B17–B27, doi: [10.1190/1.2168007](https://doi.org/10.1190/1.2168007).
- Lee, K. H., G. Liu, and H. F. Morrison, 1989, A new approach to modeling the electromagnetic response of conductive media: Geophysics, **54**, 1180–1192, doi: [10.1190/1.1442753](https://doi.org/10.1190/1.1442753).
- Maaø, F. A., 2007, Fast finite-difference time-domain modelling for marine-subsurface electromagnetic problems: Geophysics, **72**, no. 2, A19–A23, doi: [10.1190/1.2434781](https://doi.org/10.1190/1.2434781).
- Mackie, R. L., T. R. Madden, and P. E. Wannamaker, 1993, Three-dimensional magnetotelluric modeling using difference equations — Theory and comparison to integral equation solutions: Geophysics, **58**, 215–226, doi: [10.1190/1.1443407](https://doi.org/10.1190/1.1443407).
- Madden, T. R., and R. Mackie, 1989, Three-dimensional magnetotelluric modeling and inversion: Proceedings of the IEEE, **77**, 318–333, doi: [10.1109/5.18628](https://doi.org/10.1109/5.18628).
- Medina, E., A. Lovatini, F. Andreasi, S. Re, and F. Snyder, 2012, Improving subsalt imaging by incorporating MT data in a 3D earth model building workflow — A case study in Gulf of Mexico: 74th Annual International Conference and Exhibition, EAGE, Extended Abstracts, B033.
- Miensopust, M. P., P. Queralt, and A. G. Jones, , and the 3D MT modellers, 2013, Magnetotelluric 3-D inversion — A review of two successful workshops on forward and inversion code testing and comparison: Geophysical Journal International, **193**, 1216–1238, doi: [10.1093/gji/ggt066](https://doi.org/10.1093/gji/ggt066).
- Mitsuhata, Y., and T. Uchida, 2004, 3D magnetotelluric modeling using the T-Ω finite-element method: Geophysics, **69**, 108–119, doi: [10.1190/1.1649380](https://doi.org/10.1190/1.1649380).
- Mittet, R., 2010, High-order finite-difference simulations of marine CSEM surveys using a correspondence principle for wave and diffusion fields: Geophysics, **75**, no. 1, F33–F50, doi: [10.1190/1.3278525](https://doi.org/10.1190/1.3278525).
- Monk, P., and E. Sülli, 1994, A convergence analysis of Yee's scheme on nonuniform grids: SIAM Journal on Numerical Analysis, **31**, 393–412, doi: [10.1137/0731021](https://doi.org/10.1137/0731021).
- Nabighian, M. N., Ed., 2006, Electromagnetic methods in applied geophysics, vol. 1: SEG.
- Newman, G. A., and D. L. Alumbaugh, 2000, Three-dimensional magnetotelluric inversion using non-linear conjugate gradients: Geophysical Journal International, **140**, 410–424, doi: [10.1046/j.1365-246x.2000.00007.x](https://doi.org/10.1046/j.1365-246x.2000.00007.x).
- Orange, A., 1989, Magnetotelluric exploration for hydrocarbons: Proceedings of the IEEE, **77**, 287–317, doi: [10.1109/5.18627](https://doi.org/10.1109/5.18627).
- Oristaglio, M. L., and G. W. Hohmann, 1984, Diffusion of electromagnetic fields in a two-dimensional earth: Geophysics, **49**, 870–894, doi: [10.1190/1.1441733](https://doi.org/10.1190/1.1441733).
- Rickard, Y. S., and N. K. Georgieva, 2003, Problem-independent enhancement of PML ABC for the FDTD method: IEEE Transactions on Antennas and Propagation, **51**, 3002–3006, doi: [10.1109/TAP.2003.818000](https://doi.org/10.1109/TAP.2003.818000).
- Roden, J. A., and S. D. Gedney, 2000, Convolutional PML (CPML): An efficient FDTD implementation of the CFS-PML for arbitrary media: Microwave and Optical Technology Letters, **27**, 334–339, doi: [10.1002/1098-2760\(20001205\)27:5<334::AID-MOP14>3.0.CO;2-A](https://doi.org/10.1002/1098-2760(20001205)27:5<334::AID-MOP14>3.0.CO;2-A).
- Sasaki, Y., 2001, Full 3-D inversion of electromagnetic data on PC: Journal of Applied Geophysics, **46**, 45–54, doi: [10.1016/S0926-9851\(00\)00038-0](https://doi.org/10.1016/S0926-9851(00)00038-0).
- Simpson, F., and K. Bahr, 2005, Practical magnetotellurics: Cambridge University Press.
- Siripunvaraporn, W., G. Egbert, and Y. Lenbury, 2002, Numerical accuracy of magnetotelluric modeling: A comparison of finite difference approximations: Earth, Planets and Space, **54**, 721–725, doi: [10.1186/BF03351724](https://doi.org/10.1186/BF03351724).
- Sleijpen, G. L. G., and D. R. Fokkema, 1993, BiCGStab(L) for linear equations involving unsymmetric matrices with complex spectrum: Electronic Transactions on Numerical Analysis, **1**, 11–32.

- Smith, J. T., 1996, Conservative modeling of 3-D electromagnetic fields, part I: Properties and error analysis: *Geophysics*, **61**, 1308–1318, doi: [10.1190/1.1444054](https://doi.org/10.1190/1.1444054).
- Støren, T., J. J. Zach, and F. A. Maaø, 2008, Gradient calculations for 3D inversion of CSEM data using a fast finite-difference time-domain modelling code: 70th Annual International Conference and Exhibition, EAGE, Extended Abstracts, P194.
- Taflove, A., and S. G. Hagness, 2005, *The finite-difference time domain method*: Artech House.
- Titchmarsh, E. C., 1939, *The theory of functions*, 2nd ed.: Oxford University Press.
- Titchmarsh, E. C., 1948, *Introduction to the theory of Fourier integrals*, 2nd ed.: Oxford at the Clarendon Press.
- Ueda, T., and M. S. Zhdanov, 2006, Fast numerical modeling of multitransmitter electromagnetic data using multigrid quasi-linear approximation: *IEEE Transactions on Geoscience and Remote Sensing*, **44**, 1428–1434, doi: [10.1109/TGRS.2006.864386](https://doi.org/10.1109/TGRS.2006.864386).
- Vozoff, K., 1991, The magnetotelluric method, in M. N. Nabighian, ed., *Electromagnetic methods in applied geophysics*, vol. 2: SEG, 641–712.
- Wait, J., 1954, On the relation between telluric currents and the Earth's magnetic field: *Geophysics*, **19**, 281–289, doi: [10.1190/1.1437994](https://doi.org/10.1190/1.1437994).
- Wang, T., and G. Hohmann, 1993, A finite-difference, time-domain solution for three-dimensional electromagnetic modeling: *Geophysics*, **58**, 797–809, doi: [10.1190/1.1443465](https://doi.org/10.1190/1.1443465).
- Wannamaker, P. E., 1991, Advances in three-dimensional magnetotelluric modeling using integral equations: *Geophysics*, **56**, 1716–1728, doi: [10.1190/1.1442984](https://doi.org/10.1190/1.1442984).
- Weiss, C., and S. Constable, 2006, Mapping thin resistors and hydrocarbons with marine EM methods, Part II — Modeling and analysis in 3D: *Geophysics*, **71**, no. 6, G321–G332, doi: [10.1190/1.2356908](https://doi.org/10.1190/1.2356908).
- Woods, A. J., L. D. Ludeking, and D. L. Rhoades, 2010, Performance enhancement of FDTD-PIC beam-wave simulations using multi-core platforms: Presented at PIERS Progress in Electromagnetics Research Symposium, PIERS 2010, 52–55.
- Yee, K. S., 1966, Numerical solution of initial boundary value problems involving Maxwell's equations in isotropic media: *IEEE Transactions on Antennas and Propagation*, **AP-14**, 302–307, doi: [10.1109/TAP.1966.1138693](https://doi.org/10.1109/TAP.1966.1138693).